AC Conduction Mechanism in (Cu)$_x$/(CuTl)-1223 Nanoparticles–Superconductor Composites

Abrar A. Khan[1] · M. Mumtaz[1] · Liaqat Ali[1] · Mubasher[1] · Y. Slimani[2] ·
M. Nasir Khan[3] · Irfan Qasim[4]

Abstract

Copper (Cu) nanoparticles (NPs) were prepared by sol–gel process, and superconducting $(Cu_{0.5}Tl_{0.5})Ba_2Ca_2Cu_3O_{10-\delta}$ {(CuTl)-1223} phase was synthesized by conventional solid-state reaction. The desired (Cu)$_x$/(CuTl)-1223, $x = 0$–4.0 wt% composites, were obtained by adding Cu NPs in superconducting (CuTl)-1223 phase. These composites were characterized by X-ray diffraction, DC-resistivity versus temperature (R–T) and AC conduction measurements. The tetragonal crystal structure with P4/mmm space group of the host superconducting (CuTl)-1223 phase remained dominant after the addition of Cu NPs. The zero-resistivity critical temperature $T_{c(0)}$ (K) was increased, and normal state resistivity was decreased after addition of Cu NPs in CuTl-1223 phase. The frequency- and temperature-dependent AC conduction properties of (Cu)$_x$/(CuTl)-1223 composites were explored via dielectric, impedance and electric modulus measurements. The dielectric constant ($\varepsilon_r^{/}$, $\varepsilon_r^{//}$) and loss tangent (tanδ) were suppressed, while AC conductivity (σ_{ac}) was improved with the addition of Cu NPs in (CuTl)-1223 phase. Comparatively, the capacitance associated with grain boundaries regions was found to be greater than the capacitance associated with grain regions. The capacitive behavior of the grain boundaries was decreased, while that of the grains was increased with increasing operating temperature for all these composite samples. The shifting of peaks in imaginary part of the electric modulus ($M^{//}$) versus frequency (f) spectra toward lower frequency regime with increasing Cu NPs contents in superconducting (CuTl)-1223 phase is witnessed for the existence of non-Debye relaxation in the material.

Keywords (Cu)$_x$/(CuTl)-1223 composites · Cu nanoparticles · (CuTl)-1223 superconducting phase · Dielectric measurements · Complex impedance spectroscopy · Complex electric modulus spectroscopy

✉ M. Mumtaz
mmumtaz75@yahoo.com

Extended author information available on the last page of the article

1 Introduction

The key parameters for the dielectric constant of a material are capacitance, conductance, refractive index and charge screening [1]. The dielectric constant controls the screening of the electrostatic forces between the electrical charge carriers and the extra charges such as ionic impurities or oscillating dipoles in a lattice of the material [2–5]. Therefore, the dielectric response has a decisive effect on the carrier mobility, which is a fundamental property of the electronic materials. The dielectric properties of a material have a central role in the performance of the electronic devices. It is very well known that an effective dielectric material must have high dielectric constant value, low dielectric loss and high breakdown voltage. As the dielectric constant is related to the polarizability, it is strongly dependent on the chemical structure of the material [6]. The very high values of dielectric constant have also been observed in ceramics materials and high-temperature superconductors (HTSCs) [7]. In spite of the fact that the cuprate HTSCs have extensively been characterized, a very little work has been carried out on their dielectric properties. The AC conduction process in several electronic devices depends on temperature, frequency, surface charges, fabrication process and doping contents of the material. As the oxygen ions cause the space charge effects at high-temperature and low-frequency regions, the AC conduction properties (i.e., dielectric constant, impedance and modulus spectroscopies) of materials do not reflect the same intrinsic values at all frequencies and temperatures. Therefore, the study of AC conduction process over a long range of frequency and temperature is very important and is the main motivation of the current study. The frequency- and temperature-dependent AC conduction properties can provide a clue about the underlying responsible mechanism taking place in the material. The polarization mechanisms can be classified into four categories [i.e., (1) electronic polarization, (2) atomic and ionic polarization, (3) dipolar and oriental polarization and (4) interfacial polarization], which depend upon the frequency of the applied AC field [8].

In homologous $CuBa_2Ca_{n-1}Cu_nO_{2n+4-\delta}$ series of high-temperature superconductors (HTSCs), $CuBa_2Ca_2Cu_3O_{10-\delta}$ (Cu-1223) superconducting phase is extensively studied candidate because of low superconducting anisotropy ($\gamma = \xi_{ab}/\xi_c$), comparatively longer coherence length along c-axis (ξ_c) and high zero-resistivity critical temperature $T_{c(0)}$ [9]. So, these materials play a vital role in microelectronics for smaller and robust energy storage devices such as capacitors [10]. The frequency-dependent dielectric properties of $Tl_2Ba_2Ca_1Cu_2O_x$ and $Tl_2Ba_2Ca_2Cu_3O_x$ superconductors were studied at different temperatures from 80 to 300 K [11]. The values of dielectric parameters such as dielectric constants ($\varepsilon^{/}$ and $\varepsilon^{//}$), dielectric loss (tan δ) and AC conductivity (σ_{ac}) of these compounds were found to be strongly dependent on temperature and frequency of AC field. It was supposed that the dielectric response of these materials is attributable to the dipolar polarizations due to hopping of carriers. The normal state transport and dielectric properties of $Bi_{1.84}Pb_{0.34}Sr_{1.91}Ca_{2.03}Cu_{3.06}In_xO_y$ ($0 \leq x \leq 0.15$) material were investigated [12]. The increase in dielectric parameters was attributed to the increase in polarization with the increase in 'In' contents as impurity atoms in crystalline lattice sites, which can

cause deformation in surrounding volume and modification in local fields. The MgO nanoparticles-added $Cu_{0.25}Tl_{0.75}Ba_2Ca_3Cu_4O_{12-\delta}$ superconducting phase was studied for its superconducting and dielectric properties in frequency range from 100 Hz to 4 MHz at various operating temperatures from 113 to 300 K [13]. The variation in dielectric parameters was found to be strongly dependent on both frequency of external applied AC field and operating temperature values. The variation in ε'' and tan δ showed dispersion, which shifts toward lower frequencies with decreasing temperature, and such dielectric response indicated a Debye-like relaxation process in the material.

The famous tool of complex impedance spectroscopy (CIS) is mostly used to analyze the complex electrical circuits. CIS can also be used to explore the relaxation processes going on in the complex inhomogeneous systems [14, 15]. Due to its nondestructiveness, this technique is widely applied to study microstructures and their associated electrical properties [16]. For polycrystalline materials with different relaxation times, the CIS technique can be used to distinguish the contributions of grains and grain boundaries in their transport properties [17]. As persistent current flow is the key feature linked to superconductivity, CIS study of these high-temperature superconductors may help us to understand the science lying at the core of this phenomenon [5, 18].

The ceramics $CaCu_3Ti_4O_{12}$ or $Ca_{0.25}Cu_{0.75}TiO_3$ (CCTO) are extremely synthesized and characterized materials due to their unusual electrical properties [16–18]. As these CCTO materials have low loss and high dielectric constant, these compounds are very important for miniaturization of electronic devices and energy storage. $Co_{0.4}Cu_{0.2}Zn_{0.4}Al_xFe_{2-x}O_4$ material was investigated using CIS, and a decreasing trend in dielectric constant and loss tangent was observed with increasing Al content. The dielectric constant and dielectric loss were decreased in the lower frequency region and had attained constant value for the higher frequency region [19]. The AC conductivity was also decreased with increasing contents of Al due to limiting the hopping electron. The increasing hopping frequency shifted to lower frequency with increase in Al content. The electrical properties of $BaCuO_{2+\delta}$ were explored at certain selected range of frequency and temperature [20]. Nature of dielectric relaxation was observed to be non-Debye type in this compound. Both Ba_2CoNbO_6 and Sr_2CoNbO_6 ceramic materials exhibit high values of dielectric constant in low-frequency regimes at room temperature. The impedance and modulus spectra measured at room temperature over 1 Hz to 10 MHz revealed two relaxation processes with different relaxation times, which were attributed to the grain and grain boundaries [21]. The major decrease in low-frequency dielectric loss of $Y_{2/3-x}Nd_xCu_3Ti_4O_{12}$ ceramics was observed by refining the grain size after A-site Nd doping, which can be attributed to the enhanced grain boundary density [22]. The complex impedance plots of polycrystalline $KBa_2V_5O_{15}$ ceramics revealed that both the grain resistance and grain boundary resistance were decreased with the rise in temperature, which indicated the negative temperature coefficient of resistance behavior of the sample [23]. The AC electrical properties of polycrystalline $NdGaO_3$ were investigated by CIS measurements. There were two relaxation processes with different relaxation times observed from the impedance and modulus spectroscopy measurements, which were associated with the grain and the grain boundary effects.

The capacitance and resistance of grains were found to be lower than grain boundaries, and conductivity in the material was increased with temperature [24].

Modulus-based investigation of materials is equally important to gain information about electrical and other related properties of the materials. This is a convenient technique to probe dynamical processes playing part in transport properties. Mostly, this tool is applied for the determination of relaxation time and ions/carriers hopping rate [25, 26]. Commonly, the acquired experimental data are analyzed in the complex plane using impedance (Z^*), admittance (Y^*) and modulus (M^*) formalisms [27]. Complex electric modulus (CEM) is preferred over other complex formalisms when different capacitive components exist in the material and hence distribution of relaxation times comes into play. Here, for the component with minor capacitive contribution, the impedance formalism fails and modulus formalism fulfills the requirement and works well [28, 29]. In a nutshell, CEM helps in separating electrode polarization from conduction process and it also identifies components with similar resistance and different capacitances [30, 31].

The AC electrical properties of $Ni_{0.27}Cu_{0.10}Zn_{0.63}Fe_2O_4$ ceramics were studied by impedance and modulus spectroscopy. The complex impedance spectra showed both grain and grain boundary effects on the AC electrical properties. The complex modulus spectra indicated the occurrence of non-Debye type of conductivity relaxation in the material [31]. The shifting of peaks in modulus spectra of $LiNi_{1-x-y-0.02}Mg_{0.02}Co_xZn_yO_2$ ceramic material toward high-frequency regime with increasing heat input in the form of rising temperature showed thermally accelerated conduction. Multiple relaxation nature of the studied material is overall manifested by modulus analysis [32]. Complex modulus and impedance spectroscopy studies of $Ba_4SrSmTi_3V_7O_{30}$ material were carried out at different temperatures as functions of frequency. This study showed the existence of hopping mechanism, negative temperature coefficient of resistance (NTCR) and non-Debye relaxation in the material [33]. Impedance and modulus formalisms were applied to characterize ZrO_2–TiO_2–V_2O_5 nanocomposites. Shifting of peaks toward higher frequency with temperature is an evidence of thermally accelerated conduction in these nanocomposites. A non-Debye-type relaxation process was revealed by both impedance and modulus formalisms [34]. The modulus study of Ag_2O–CdI_2–CdO nanocomposites showed the temperature-independent and composition-dependent electrical relaxation of Ag^+ ions in these nanocomposites. It was observed that the activation energy for conduction was increased and total AC conductivity was decreased with increasing Ag_2O content in this material [35].

The main objective of this study was to figure out the different factors contributing to the energy dissipation in the material, e.g., grain boundaries, grains, impurities, etc., which can be rectified in future by minimizing their contribution in energy dissipation. As the superconducting properties can be improved by reducing the energy dissipation, the factors contributing to energy dissipation must be explored and addressed. The present study has been carried out to investigate the electrical AC conduction mechanism of $(Cu)_x/(CuTl)$-1223 composites. The outcomes of this work will help and guide the audience in acquiring the relevant information about relaxation time and amplitude of relaxation associated with several processes going on in these composites. The prime focus of this study is to bring out the effects of

Cu NPs incorporation in (CuTl)-1223 superconducting phase by observing and analyzing dielectric, impedance and capacitive contribution in AC conduction process. For the said purpose, the material was tested by varying its composition, test frequency and temperature. This study will give insight to the readers about the role of different factors contributing to electrical transport properties of the system.

2 Samples Synthesis and Experimental Details

The calculated quantities of $Cu_2(CN)_2$, $Ca(NO_3)_2$ and $Ba(NO_3)_2$ chemicals were weighed by electronic digital balance and ground for nearly two hours in agate mortar and pestle. This ground mixture was then put into preheated chamber furnace for 24-h heat treatment at 860 °C. The furnace was switched off after 24-h heat treatment and allowed to cool the material to room temperature. This process of heat treatment was repeated following intermediate grinding for 1 h. Then, Cu NPs synthesized by sol–gel process and calculated quantity of thallium oxide (Tl_2O_3) were added into the precursor material. The round-shaped pellets of the final mixed and ground material were prepared with the help of hydraulic press. At the final stage, these pellets enclosed in gold capsules were sintered at 860 °C for 10 min to obtain $(Cu)_x/(CuTl)$-1223, $x = 0$, 1.0, 2.0, 3.0 and 4.0 wt% composites.

The structure and phase purity of Cu NPs and $(Cu)_x/(CuTl)$-1223 composites were probed by XRD (D/Max IIIC Rigaku with CuKα source of X-rays with wavelength 1.54056 Å). The DC-resistivity (ρ) versus temperature T (K) measurements of these composites were carried out by four-point probe method. The 9 Tesla Physical Property Measurement System (PPMS) Superconducting Magnet (SCM6) from Quantum Design was used for these R–T measurements. The frequency-dependent dielectric, impedance and modulus measurements of these composites were carried out at different operating temperatures by LCR meter (Hewlett-Packard 4294A). The thin layers of silver paint were applied on both the surfaces of the rectangular-shaped sample and dried at room temperature to make them conducting electrode surfaces for frequency-dependent dielectric, impedance and modulus measurements by conventional two-point probe method.

3 Results and Discussion

3.1 X-Rays Diffraction (XRD)

The phase purity and crystal structure of Cu NPs were investigated using XRD as shown in Fig. 1. Average crystallite size of Cu NPs calculated by Scherer's formula was found to be 20 nm. The XRD peaks found at 43.09°, 50.32° and 74.15° were indexed as (111), (200) and (220) planes according to the standard JCPDS card (Card No. 04-0836) indicating FCC crystal structure of these Cu NPs [36, 37]. The XRD spectra of representative $(Cu)_x/(CuTl)$-1223, $x = 0$ and 4.0 wt% composites, are shown in Fig. 2. The most of the diffraction peaks were indexed showing the tetragonal crystal structure with P4/mmm space group. Some of the diffraction peaks of

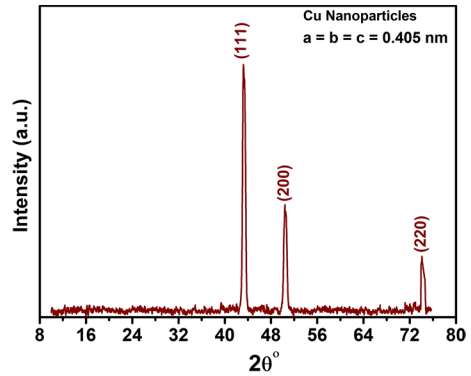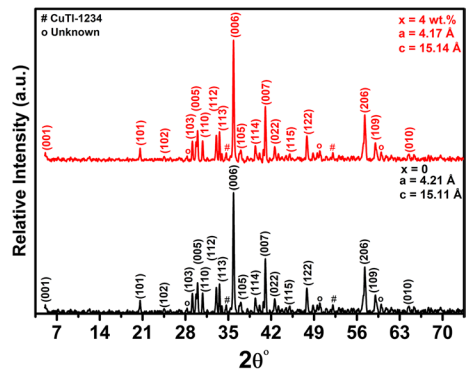**Fig. 1** XRD spectrum of Cu nanoparticles (Color figure online)

Fig. 2 Representative XRD spectra of $(Cu)_x$/CuTl-1223, $x=0$ and 4.0 wt.% nanoparticles–superconductor composites (Color figure online)


small intensity were also observed that were marked as impurities and some other superconducting phases present in these composites. The unchanged crystal structure of the host CuTl-1223 superconducting matrix with the addition of these Cu nanoparticles confirms that they have been dispersed over the intergranular spaces of the host CuTl-1223 matrix. Moreover, the sizes of these Cu nanoparticles are larger than the unit cell size of CuTl-1223 superconducting phase. For atomic substitution inside the crystal structure of the host CuTl-1223 matrix, these Cu nanoparticles have to be thermally decomposed into atoms. Since the synthesis temperature (i.e., 860 °C) of these samples is very low as compared to the decomposition temperature (i.e., 1083 °C) of Cu nanoparticles, the chances of entrance of atoms of these nanoparticles inside the crystal structure of host CuTl-1223 matrix are negligible.

3.2 Resistivity Versus Temperature Measurements

The representative graphs showing the variation in DC-resistivity ρ (Ω m) with temperature T (K) for $(Cu)_x$/(CuTl)-1223, $x=0$ and 4.0 wt% composites, are given in Fig. 3. The normal state resistivity ρ_n(Ω-m) was decreased from 1.76×10^{-2} to 9.21×10^{-3} Ω m, and the value of $T_{c(0)}$ (K) was increased from 98 to 108 K for

Fig. 3 Resistivity versus temperature (*RT*) measurements of $(Cu)_x$/CuTl-1223, $x = 0$ and 4.0 wt% nanoparticles–superconductor composites (Color figure online)
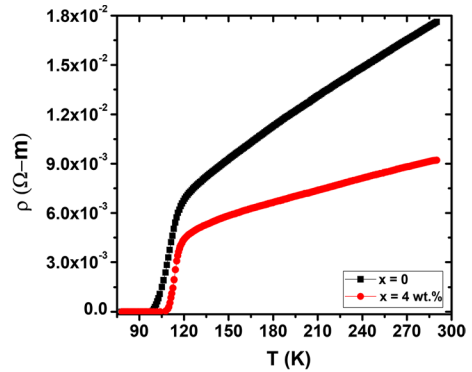
$(Cu)_x$/(CuTl)-1223 composites with $x = 0$ and 4.0 wt% of Cu NPs. This improvement in the superconducting parameters was attributed to the enhancement of intergrain coupling and reduction of potential barriers to the carrier's mobility across the grain boundaries due to the presence of conducting natured Cu nanoparticles spread over the intergranular spaces of (CuTl)-1223 superconductor phase.

3.3 Complex Dielectric Measurements

The frequency-dependent dielectric properties of $(Cu)_x$/(CuTl)-1223, $x = 0$–4.0 wt% composites, were investigated from 40 Hz to 100 MHz at different temperatures from 78 to 253 K. The dielectric parameters such as ε_r', ε_r'', $\tan\delta$ and σ_{ac} were measured, compared and explained in the light of available literature. These are the parameters which fix the basic criterion for the selection of any material for practical dielectric applications. When the dielectric material in parallel plate capacitor is subjected to the oscillating electric field $E = E_o\,e^{j\omega t}$, then the displacement of the charges due to the oscillating electric field with phase difference of δ is $D = D_o\,e^{j(\omega t - \delta)}$, which gives the complex permittivity as in Eq. (1) [38]:

$$
\begin{aligned}
\varepsilon_r^* &= \frac{D_o}{E} e^{j(\omega t - \delta)} \\
&= \varepsilon_r' - j\varepsilon_r'' \\
&= \frac{1}{j\omega C_o Z^*}
\end{aligned}
\tag{1}
$$

where $j = \sqrt{-1}$, $Z^* = V^*/I^*$, V^* and I^* are the applied AC voltage and AC current to the samples, respectively. Also $C_o = \varepsilon_o A/d$ with ε_o is permittivity of free space, A is area and d is thickness of the samples.

The real part of dielectric constant (ε_r') is given by Eq. (2) [38]:

$$
\varepsilon_r' = \frac{D_o}{E} \cos\theta,
\tag{2}
$$

and imaginary part of dielectric constant (ε_r'') is given by Eq. (3) [38]:

$$\varepsilon_r^{//} = \frac{D_o}{E} \sin\theta \qquad (3)$$

The values of $\varepsilon_r^{/}$ and $\varepsilon_r^{//}$ depend upon the two characteristics of the material, first one is charge storage (i.e., capacitive nature of material) and second is charge transfer (i.e., conductive nature of material) [39]. The dielectric phenomenon in ferrites and polycrystalline HTSCs has been best explained by the Koop's theory and Maxwell–Wagner model [40, 41]. According to these models, there are two distinct regions in the polycrystalline materials, i.e., good conducting grains and poor conducting grain boundaries. The charges reach from grain to grain boundaries by the hopping mechanism when electric field is applied to polycrystalline sample. These dielectric properties have been investigated at different constant operating temperatures from normal state of the samples at room temperature to their superconducting state. The lower thermal agitation at lower temperature may enhance the polarizability of the atoms and hence their dielectric constants. The dielectric constants $\varepsilon^{/}$ and $\varepsilon^{//}$ are most likely arising from the dielectric polarization originating from the displacement of mobile electronic charges present in the conducting grains from the equilibrium position relative to the grain boundaries. At higher frequencies, the dielectric polarization arising from the displacement of mobile carriers in conducting grains relative to the grain boundaries is negligible, and the values of dielectric constants approach to negligible values. The capacitance due to dipolarization is modeled to be originating from the displacement of mobile carriers in conducting grains from their equilibrium position relative to the relatively static charges across the grain boundaries. The variation in $\varepsilon_r^{/}$ with frequency at different temperatures of $(Cu)_x/(CuTl)$-1223 composites is shown in Fig. 4a–e. The combined graph showing the variation in $\varepsilon_{r(max.)}^{/}$ with T (K) at 40 Hz is given in Fig. 4f. The maximum value of $\varepsilon_r^{/}$ was observed at lower frequencies, which can be associated with interfacial polarization [39]. The value of $\varepsilon_r^{/}$ was gradually decreased with the increase in frequency and became constant having very small value at certain high frequency. The dielectric constant was decreased at high frequencies due to lagging of carriers across the grain boundaries. The charge carriers cannot follow the frequency at high values as the time required by carriers to oscillate with external AC field becomes shorter and hence the response of the material to polarization becomes very small. A resonance and anti-resonance in the graphs of $\varepsilon_r^{/}$ versus f (Hz) were observed around 10^7 Hz for all the samples, which was mostly associated with carrier relaxations and physical barriers that restrain charge migrations [42]. The values of $\varepsilon_r^{/}$ were increased with the increase in temperature and were decreased with the increase in Cu NPs contents. This increase in $\varepsilon_r^{/}$ with T (K) was due to orientational polarization associated with thermal motions of molecules as dipoles cannot orient themselves at relatively lower temperatures [42–44]. The highest values of $\varepsilon_r^{/}$ at 40 Hz are 2.74×10^4, 9.84×10^3, 3.87×10^3, 2.84×10^3 and 7.80×10^3 for $(Cu)_x/(CuTl)$-1223 composites with $x = 0$, 1, 2, 3 and 4 wt%, respectively. The maximum values of $\varepsilon_r^{/}$ at 40 Hz were decreased with increasing Cu NPs contents in (CuTl)-1223 superconducting matrix. The decrease in the values of $\varepsilon_r^{/}$ with increasing contents of Cu NPs can be associated with less polarization due to enhanced conducting
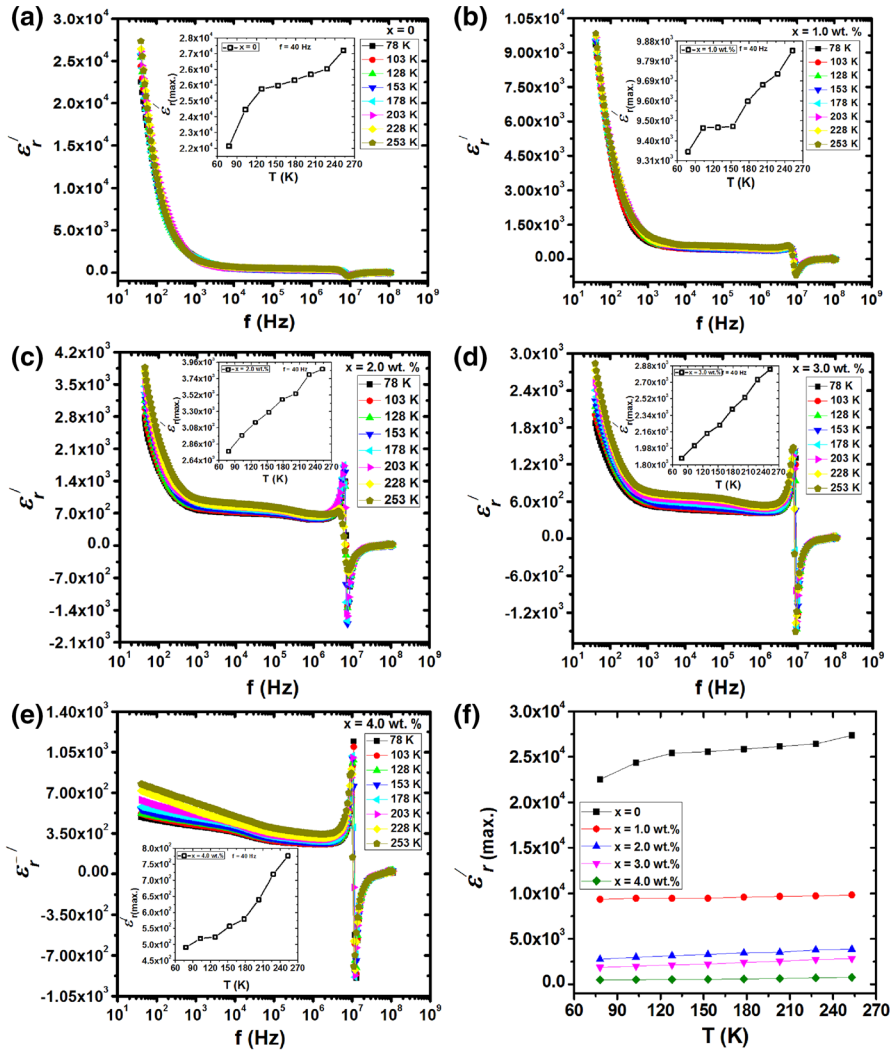
Fig. 4 Variation in the real part of dielectric constant (ε_r') with the frequency f (Hz) from 40 Hz to 10 MHz and T (K) from 78 to 253 K of $(Cu)_x$/CuTl-1223 nanoparticles–superconductor composites with **a** $x=0$, **b** $x=1.0$ wt%, **c** $x=2.0$ wt%, **d** $x=3.0$ wt%, **e** $x=4.0$ wt% (the insets show the variation in (ε_r') versus operating temperature (T) at frequency of 40 Hz), and **f** the variation in $\varepsilon_{r(max)}'$ with the operating temperature T (K) of $(Cu)_x$/CuTl-1223, $x=0$, 1.0, 2.0, 3.0 and 4.0 wt%, nanoparticles–superconductor composites (Color figure online)

nature of grain boundaries promoted by the presence of these conducting Cu NPs there, which can ease the mobility of carriers across the grain boundaries.

The variation in the imaginary part of the dielectric constant (ε_r'') with frequency f (Hz) at various values of T (K) from 78 to 253 K of $(Cu)_x$/(CuTl)-1223 composites with (a) $x=0$, (b) $x=1.0$ wt% (c) $x=2.0$ wt% (d) $x=3.0$ wt%, (e) $x=4.0$ wt% is shown in Fig. 5a–e. In the insets of Fig. 5a–e, the variation in $\varepsilon_{r(max)}''$ versus operating
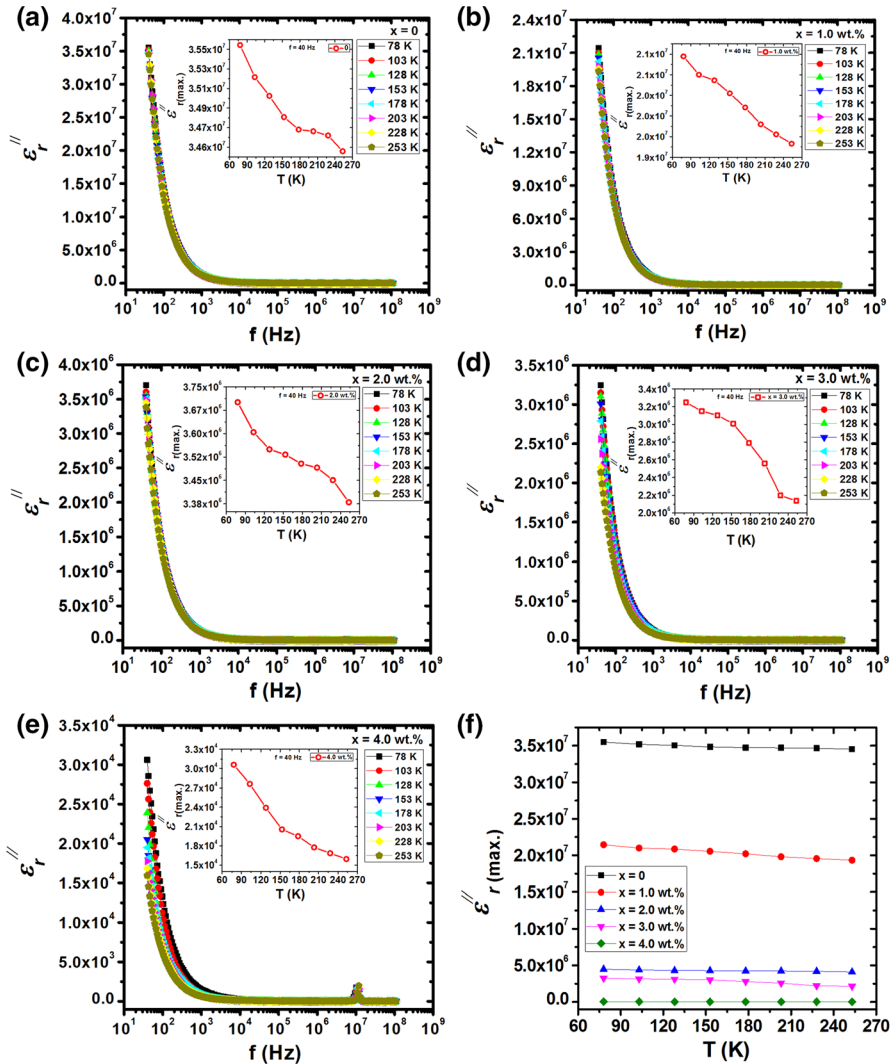
Fig. 5 Variation in the imaginary part of the dielectric constant (ε_r'') with the frequency f (Hz) from 40 Hz to 10 MHz and T (K) from 78 to 253 K of $(Cu)_x$/CuTl-1223 nanoparticles–superconductor composites with **a** $x=0$, **b** $x=1.0$ wt%, **c** $x=2.0$ wt%, **d** $x=3.0$ wt%, **e** $x=4.0$ wt% (the insets show the variation in (ε_r'') versus operating temperature (T) at frequency of 40 Hz), and **f** the variation in $\varepsilon_{r(max)}''$ with the operating temperature T (K) of $(Cu)_x$/CuTl-1223, $x=0$, 1.0, 2.0, 3.0 and 4.0 wt%, nanoparticles–superconductor composites (Color figure online)

temperature T (K) at frequency of 40 Hz is shown. The variation in $\varepsilon_{r(max)}''$ versus T (K) at frequency of 40 Hz is shown in Fig. 5f to compare the variation in $\varepsilon_{r(max)}''$ with Cu nanoparticles contents in $(Cu)_x$/(CuTl)-1223 composites. The energy loss in the material exposed to external applied AC field represented by ε_r'' arises from different mechanisms such as conduction, vibrational and dipole losses [43]. The energy loss due to

conduction process is associated with transformation of ion over large distance. These ions have also the ability to jump over a potential barrier and transfer some part of energy to the lattice in the form of heat. The values of $\varepsilon_r^{//}$ were diminished with increasing frequency, which became constant at higher frequency due to difference in time period of charge carriers and applied AC field. The second possible reason for the decrease in $\varepsilon_r^{//}$ at higher frequencies was the reduction of orientational and space charge polarizations, which are the main sources of polarization in these materials. The values of $\varepsilon_r^{//}$ were reduced with the rise in temperature and increase in Cu NPs concentration. The highest values of $\varepsilon_r^{//}$ at lowest possible applied frequency of 40 Hz are 3.45×10^7, 1.93×10^7, 3.39×10^6, 2.14×10^6 and 1.59×10^4 at room temperature of 253 K for $(Cu)_x/$ (CuTl)-1223 samples with $x = 0$, 1, 2, 3 and 4 wt% Cu NPs contents, respectively. The maximum values of $\varepsilon_r^{//}$ were decreased with the inclusion of conducting natured Cu NPs, which could facilitate the mobility of carriers across the grain boundaries and as a result reduced the polarizability in the material.

The net energy loss in the material is commonly referred as loss tangent 'tanδ.' It is obtained by taking the ratio of $\varepsilon_r^{/}$ and $\varepsilon_r^{//}$ that is given by [38];

$$\tan \delta = \varepsilon_r^{//} / \varepsilon_r^{/} \tag{4}$$

The variation in tanδ versus f (Hz) at different temperatures from superconducting state to normal state of these composites is shown in Fig. 6a–e. The variation in maximum values of tanδ with T (K) at 40 Hz for different concentrations of Cu NPs in (CuTl)-1223 superconducting phase is shown in Fig. 6f. The maximal values of tanδ at 253 K and 40 Hz are 6.35×10^3, 4.30×10^3, 1.38×10^3, 1.04×10^3 and 2.10×10^1 for $(Cu)_x/(CuTl)$-1223 samples with $x = 0$, 1, 2, 3 and 4 wt%, respectively. It was observed that the maximal values of tanδ at 40 Hz were decreased with increasing T (K) from 78 to 253 K as shown Fig. 6f. It was also observed that the maximal values of tanδ were also reduced with increasing contents of Cu NPs in (CuTl)-1223 matrix at all operating temperatures. A decreasing trend in tanδ was observed with increasing frequency, and its values became very small and almost constant at certain higher frequencies for all the samples. A resonance and anti-resonance in the graphs of tanδ versus f (Hz) were also observed around 10^7 Hz for all the samples, which was mostly associated with carriers relaxations and physical barriers that restrain charge migrations [42]. The gradual decrease in the values of tanδ with increasing values of frequency was associated with the difference in time constants of charge carriers and applied AC field. Overall decreasing trend in tanδ with increasing Cu NPs contents can be associated with metallic nature of these NPs. The values of tanδ were also found to decrease with the rise in temperature due to enhanced polarizability. The decrease in the values of tanδ with increasing temperature may be due to larger energy stored than energy loss.

The AC conductivity (σ_{ac}) can be calculated by the following mathematical relation [38]:

$$\sigma_{ac} = \omega \varepsilon_r^{/} \varepsilon_o D \tag{5}$$

where $D = \tan\delta$ is dissipation factor. The variation in σ_{ac} with f (Hz) at different values of T (K) is shown in Fig. 7a–e, and the variation in maximum AC conductivity
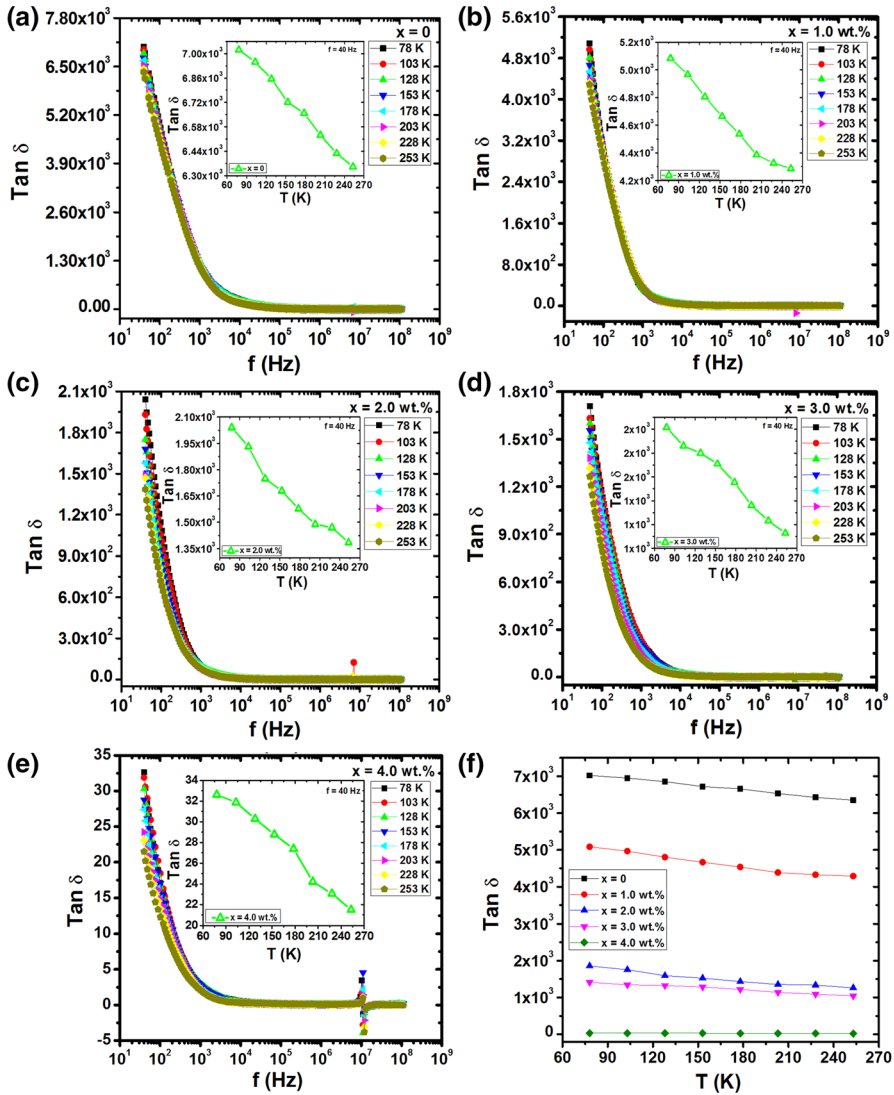
Fig. 6 Variation in the loss tangent (tanδ) with frequency f (Hz) from 40 Hz to 10 MHz and T (K) from 78 to 253 K of $(Cu)_x$/CuTl-1223 nanoparticles–superconductor composites with **a** $x=0$, **b** $x=1.0$ wt%, **c** $x=2.0$ wt%, **d** $x=3.0$ wt%, **e** $x=4.0$ wt%, and **f** the variation in the maximum tanδ with the operating temperature T (K) of $(Cu)_x$/CuTl-1223, $x=0$, 1.0, 2.0, 3.0 and 4.0 wt. %, nanoparticles–superconductor composites (Color figure online)

$\sigma_{ac(max.)}$(Sm^{-1}) with T (K) at frequency 2×10^7 Hz for $(Cu)_x$/(CuTl)-1223 samples is shown in Fig. 7f. The value of σ_{ac} was small at lower frequency due to small number of free charge carriers available for conduction as most of the charge carriers were trapped across potential barriers at the grain boundaries [44]. The carriers piled up across the grain boundaries at lower frequencies causing maximum polarization in
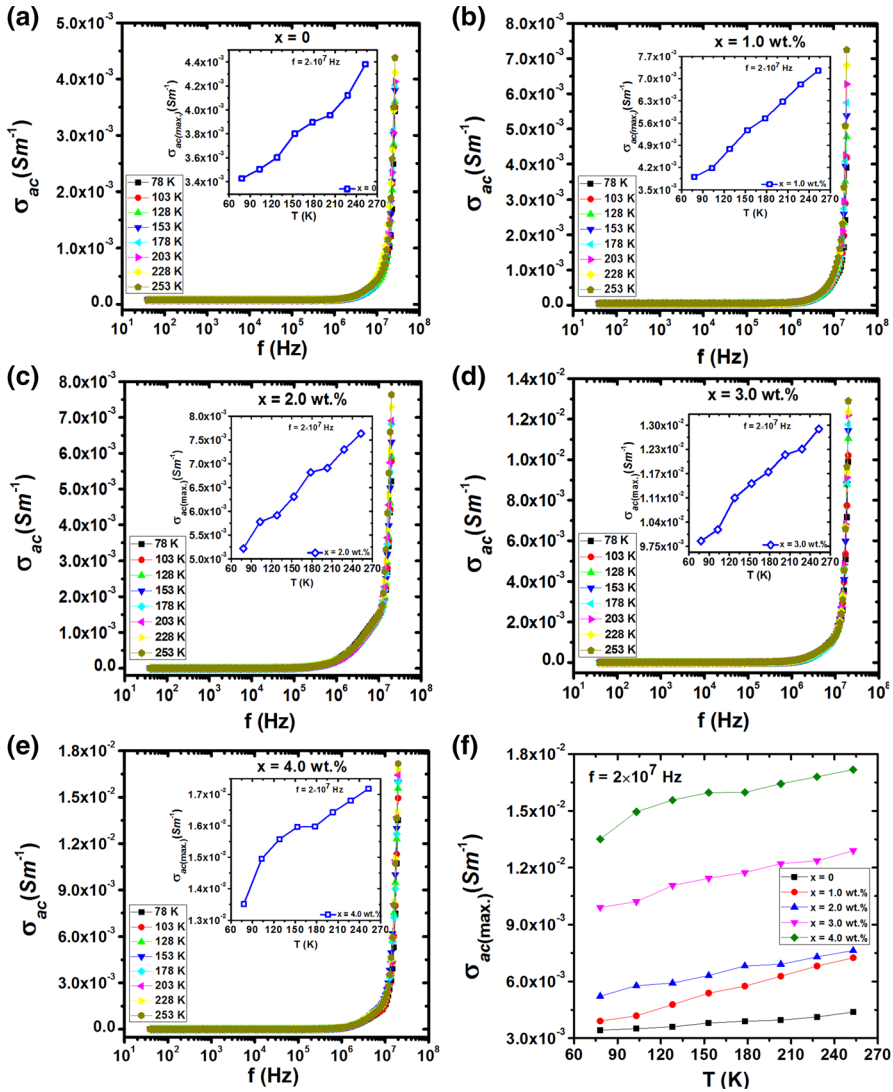
Fig. 7 Variation in the AC conductivity (σ_{ac}) with frequency f (Hz) from 40 Hz to 10 MHz and T (K) from 78 to 253 K of $(Cu)_x$/CuTl-1223 nanoparticles–superconductor composites with **a** $x=0$, **b** $x=1.0$ wt%, **c** $x=2.0$ wt%, **d** $x=3.0$ wt%, **e** $x=4.0$ wt%, and **f** the variation in the maximum σ_{ac} with the operating temperature T (K) of $(Cu)_x$/CuTl-1223, $x=0$, 1.0, 2.0, 3.0 and 4.0 wt%, nanoparticles–superconductor composites (Color figure online)

the material. The value of σ_{ac} started increasing with the increase in frequency due to greater number of responding carriers with greater energy and less barrier height. The value of $\sigma_{ac(max.)}(Sm^{-1})$ at 2×10^7 Hz was increased with increasing temperature T (K) for all the samples. The values of $\sigma_{ac(max.)}(Sm^{-1})$ at 253 K and 2×10^7 Hz are 4.38×10^{-3}, 7.25×10^{-3}, 7.63×10^{-3}, 1.29×10^{-2} and 1.71×10^{-2} Sm^{-1} for $(Cu)_x$/

(CuTl)-1223 composites with $x=0$, 1.0, 2.0, 3.0 and 4.0 wt.%, respectively. The increase in σ_{ac} with increasing temperature can be associated with availability of excess carriers due to thermal vibrations and activation of charge carriers [45]. The increase in the values σ_{ac} with increasing Cu NPs contents in (CuTl)-1223 matrix is an evidence of improved intergrain connections, which could ease the mobility of carriers across the potential barrier of grain boundaries. The increase in the values of σ_{ac} with increasing Cu NPs contents at intergranular spaces indicated that the nature of grain boundaries was changed due to the presence of these metallic Cu NPs there in (CuTl)-1223 matrix.

3.4 Complex Impedance Spectroscopy (CIS)

Complex impedance spectroscopy (CIS) has been effectively used to probe the electrical transport properties of different polycrystalline materials, which reveals the homogeneous or inhomogeneous nature of polycrystalline materials. This technique helps to describe the electrical relaxation as microscopic property in ionic solids at different values of frequencies and temperatures. The dynamics of bound charge carriers in the bulk or at interfacial sites of the polycrystalline materials can be investigated by using CIS [46]. Through CIS, a direct correlation between an idealized model circuit and real system comprising of electrical components of discrete nature can easily be drawn [47]. An equivalent circuit based on impedance spectra has been designed, which gives physical information about the processes taking place inside the material. As most of the ceramics contain two types of regions, namely grains and grain boundaries, CIS helps to differentiate between individual contributions of both these regions [48]. CIS is also considered as significant and easy-to-handle tool for the determination and analysis of electrical transport phenomenon [49]. Thus, we have designed an equivalent circuit to examine that how grain boundaries and the grains are taking part in AC conduction process in the material. The grains' resistance (R_g) parallel to grains' capacitance (C_g) is joined in series with grain boundaries' resistance (R_{gb}), parallel to grain boundaries' capacitance (C_{gb}) in the electrical circuit shown in Fig. 8f. The complex impedance (Z^*) in terms of real and imaginary parts can be described as

$$Z^* = Z'_{real} + jZ''_{imag} \tag{6}$$

where Z' and Z'' are the real and imaginary parts of complex impedance Z^*:

$$Z' = \left(\frac{R_g}{1 + (\omega C_g R_g)^2} \right) + \left(\frac{R_{gb}}{1 + (\omega C_{gb} R_{gb})^2} \right) \tag{7}$$

$$Z'' = R_g \left(\frac{\omega C_g R_g}{1 + (\omega C_g R_g)^2} \right) + R_{gb} \left(\frac{\omega C_{gb} R_{gb}}{1 + (\omega C_{gb} R_{gb})^2} \right) \tag{8}$$
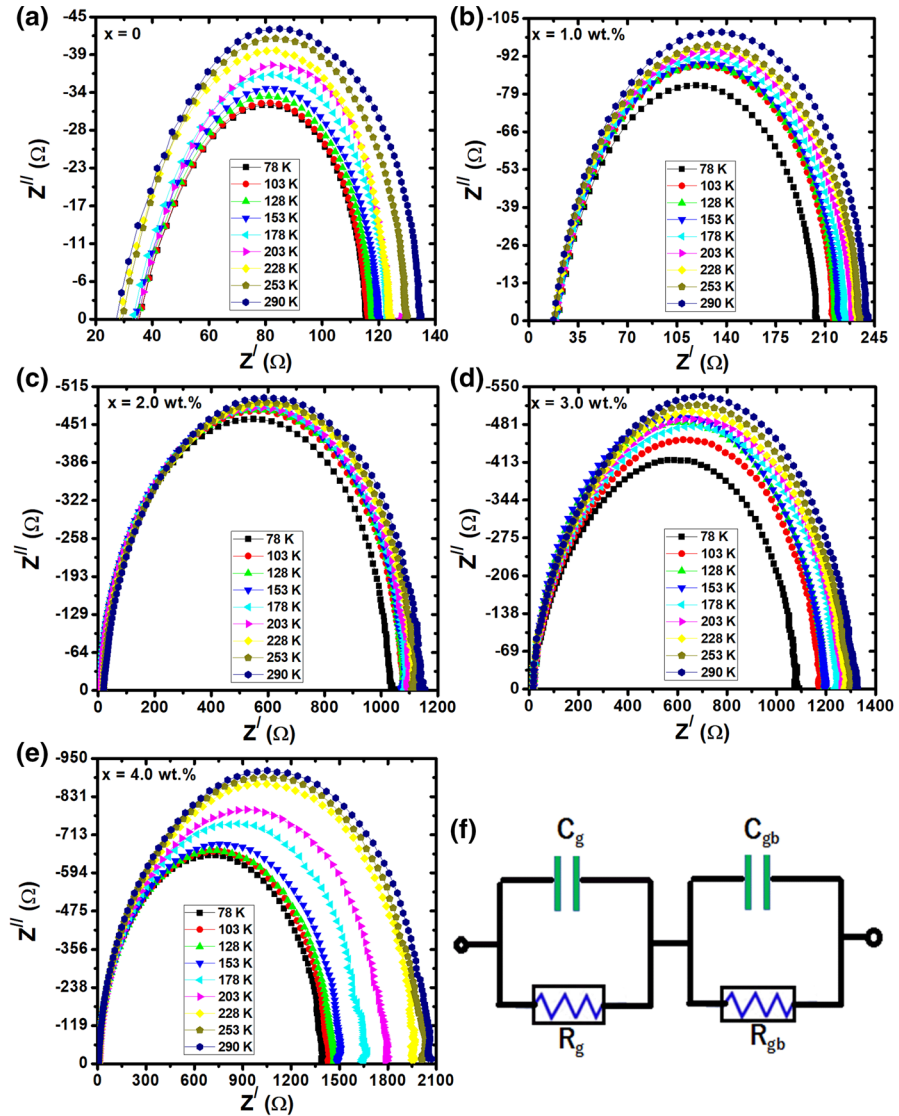
Fig. 8 Nyquist plots of real $Z^{/}$ (Ω) versus imaginary $Z^{//}$ (Ω) parts of impedance for $(Cu)_x$/CuTl-1223 composites with **a** $x=0$ at $T=78$–290 K, **b** $x=1.0$ wt% at $T=78$–290 K, **c** $x=2.0$ wt% at $T=78$–290 K, **d** $x=3.0$ wt% at $T=78$–290 K, **e** $x=4.0$ wt% at $T=78$–290 K and **f** electrical equivalent circuit for complex impedance (Color figure online)

The Nyquist plots of $Z^{/}$ (Ω) versus $Z^{//}$ (Ω) at different values T (K) for $(Cu)_x$/CuTl-1223 composites in frequency range from 40 Hz to 100 MHz are shown in Fig. 8a–e. The values of R_g and R_{gb} can easily be deduced from impedance spectrum as R_g can be obtained from left intercept, while net resistance ($R=R_{gb}+R_g$) can be obtained from

right intercept with Z'-axis of the Nyquist plots. The following mathematical relations (9) and (10) can be used to calculate the values of C_g and C_{gb}, respectively:

$$f\text{max} = \frac{1}{2\pi R_g C_g} \tag{9}$$

$$f\text{max} = \frac{1}{2\pi R_{gb} C_{gb}} \tag{10}$$

The values of 'R_g' and 'R_{gb}' are given in Table 1. The growing resistive response of both grains and grain boundaries with increasing temperature is an evidence of their conducting nature. The greater values of 'R_{gb}' as compared to the values of 'R_g' demonstrate that the grain boundaries are more resistive than grains. The most likely reason is the presence of different defects and nonstoichiometric distribution of oxygen across the grain boundaries.

The noticeable change in the shapes of Nyquist plots with increase in temperature clearly suggested a change in the value of resistance with temperature that indicates the occurrence of multi-Debye relaxation phenomena in the material. The value of total resistance of $(Cu)_x$/CuTl-1223 composites was found to increase with the increase in temperature as given in Table 1. The most likely reason for the increase in total resistance with temperature is the increase in defects like oxygen vacancies and space charges across the grain boundaries of the material [41, 50]. The mobility of carriers between the grains and grain boundaries can be affected by the presence of these defects due to trapping of carriers across the potential wells at intergranular sites promoting the resistive behavior of the material.

The small polaron hopping (SPH) model was used to calculate the activation energy of carriers by using Eq. (11) as follows:

$$\frac{R}{T} = A_o e^{\frac{E_a}{kT}} \tag{11}$$

Table 1 Calculated values of 'R_g' and 'R_{gb}' of $(Cu)_x$/CuTl-1223, $x=0$, 1.0, 2.0, 3.0 and 4.0 wt% nanoparticles–superconductor composites at various temperatures from 78 to 290 K
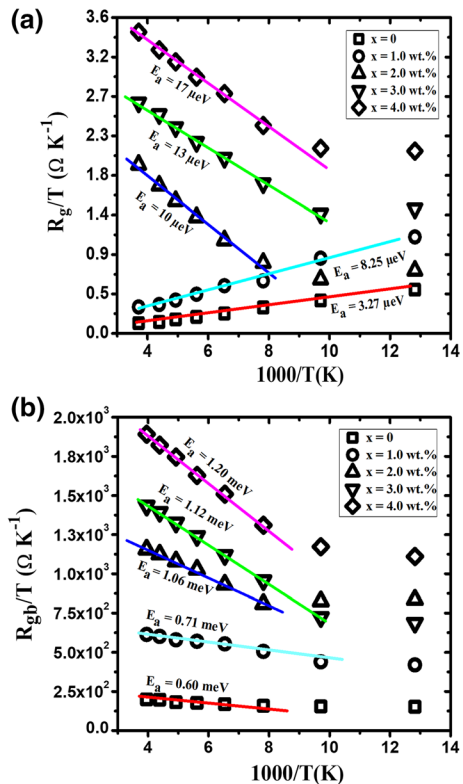
T (K)	$(Cu)_x$/CuTl-1223 composites									
	$x=0$		$x=1.0$ wt%		$x=2.0$ wt%		$x=3.0$ wt%		$x=4.0$ wt%	
	R_g	R_{gb}	R_g	R_{gb}	R_g	R_{gb}	R_g	R_{gb}	R_g	R_{gb}
78	33.2	87	20.1	182	7.1	1042	9.11	1083	7.1	1383
103	33.1	88	20.6	194	7.2	1068	9.38	1189	7.2	1425
128	32.7	85	20.8	196	7.4	1080	9.58	1193	7.4	1460
153	32.8	87	20.3	198	8.3	1071	9.81	1195	8.3	1478
178	32.7	90	19.6	204	8.5	1078	9.88	1248	8.5	1638
203	31.6	92	20.3	208	8.6	1092	10.2	1266	8.6	1781
228	32.2	91	19.5	213	8.7	1106	10.5	1274	8.7	1952
253	27.5	95	19.1	214	8.2	1123	10.7	1303	8.2	2007
290	27.9	100	19.5	220	8.9	1135	11.2	1309	8.9	2047

,Here R, A_o, k and E_a are resistance, pre-exponential factor, Boltzmann's constant and activation energy, respectively [51]. The variation in calculated activation energies for grains and grain boundaries versus Cu NPs contents in (CuTl)-1223 matrix is shown in Fig. 9a, b. The values of E_a calculated for grains are 3.27 μeV, 8.25 μeV, 10 μe V, 13 μeV and 17 μeV, and those for grains boundaries are 0.60 meV, 0.71 meV, 1.06 meV, 1.12 meV and 1.2 meV for $(Cu)_x$/(CuTl)-1223 composites with $x=0$, 1.0, 2.0, 3.0 and 4.0 wt% of Cu NPs contents, respectively. The increase in activation energy manifests that the AC conduction mechanism in the material is thermally activated [52]. The carriers can be blocked at internal interfaces in polycrystalline materials (having grains and grain boundaries) due to the presence of different microstructural imperfections such as cracks, pores, etc [53]. The blocking factor (α_R) demonstrates the contribution of grain boundaries to the overall AC conductivity of material and can be estimated quantitatively by Eq. (12) given below:

$$\alpha_R = \frac{R_{gb}}{R_g + R_{gb}} \tag{12}$$

The value of α_R gives the information about the fraction of blocked charge carriers across the potential wells at grain boundaries in the material. The variation in α_R

Fig. 9 **a** Plots of R_g/T ($\Omega\ K^{-1}$) versus $1000/T$ (K) for $(Cu)_x$/CuTl-1223, $x=0$, 1.0, 2.0, 3.0 and 4.0 wt% composites, **b** the plots of R_{gb}/T ($\Omega\ K^{-1}$) versus $1000/T$ (K) for $(Cu)_x$/CuTl-1223, $x=0$, 1.0, 2.0, 3.0 and 4.0 wt% composites (Color figure online)

with T (K) for $(Cu)_x$/(CuTl)-1223 composites is shown in Fig. 10. The percentage value of α_R is increased with increasing Cu NPs content in CuTl-1223 matrix.

The variation in Z' (Ω) versus f (Hz) at various T (K) from 78 to 290 K for $(Cu)_x$/(CuTl)-1223 composites is shown in Fig. 11a–e. The information from these plots can be useful to understand the dynamics of carriers' mobility in the material. The high values of Z' (Ω) in the low-frequency region show maximum resistive behavior of the material. The charge carriers are trapped in potential wells across the grain boundaries at low-frequency regions giving excess dielectric parameters. The charge carriers can easily follow the external applied AC electric field, which depends on the frequency and time constant of the interface states [54]. All the curves of Z' (Ω) versus f (Hz) overlap regardless of T (K) at high frequency, which can be associated with absence of restoring force leading to the mobility of carriers under the influence of an induced electric field. The gradual increase in the value of Z' (Ω) with the increase in T (K) is evident from the graphs showing the variation in Z' (Ω) versus T (K) at 40 Hz as given in the insets of Fig. 11a–e. The combined graph showing the variation in Z' (Ω) with T (K) at 40 Hz for $(Cu)_x$/(CuTl)-1223 composites is given in Fig. 11f. The value of Z' (Ω) has overall been enhanced after addition of Cu NPs in CuTl-1223 matrix. The maximum values of Z' (Ω) at 40 Hz varied from 1.16×10^2 to 1.37×10^2, 2.04×10^2 to 2.40×10^3, 1.03×10^3 to 1.14×10^3, 1.07×10^3 to 1.37×10^3 and 1.39×10^3 to 2.07×10^3 at temperature from 78 to 290 K for $(Cu)_x$/(CuTl)-1223 composites with $x = 0$, 1.0, 2.0, 3.0 and 4.0 wt% of Cu NPS, respectively. The increase in Z' (Ω) with T (K) is probably due to increase in the resistive behavior of the grain boundaries, which shows the conducting nature of grain boundaries further promoted by the addition of conducting Cu NPs in (CuTl)-1223 matrix.

The graphs of Z'' (Ω) versus f (Hz) at various T (K) values from 78 to 290 K for $(Cu)_x$/(CuTl)-1223 composites are shown in Fig. 12a–e. It is noticed from these graphs that the value of Z'' (Ω) was increased with the increase in the value of frequency f (Hz) and reached at its maximum value Z''_{max} (Ω) for all the samples at all T (K) values. The graphs showing the variation in Z''_{max} (Ω) versus T (K) are given in the insets of Fig. 12a–e, which shows the gradual increase in the values of Z''_{max} (Ω) with increasing T (K) values. The values of Z''_{max} (Ω) are found

Fig. 10 Blocking factor (α_R) as a function of temperature for $(Cu)_x$/CuTl-1223, $x = 0$, 1.0, 2.0, 3.0 and 4.0 wt% composites (Color figure online)
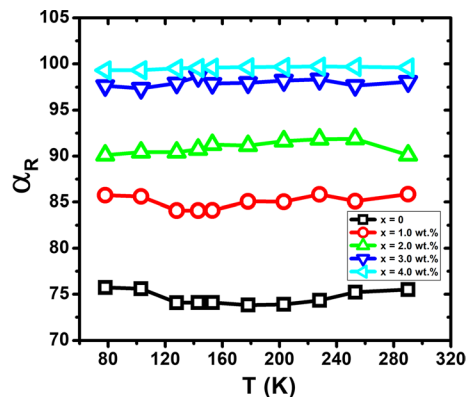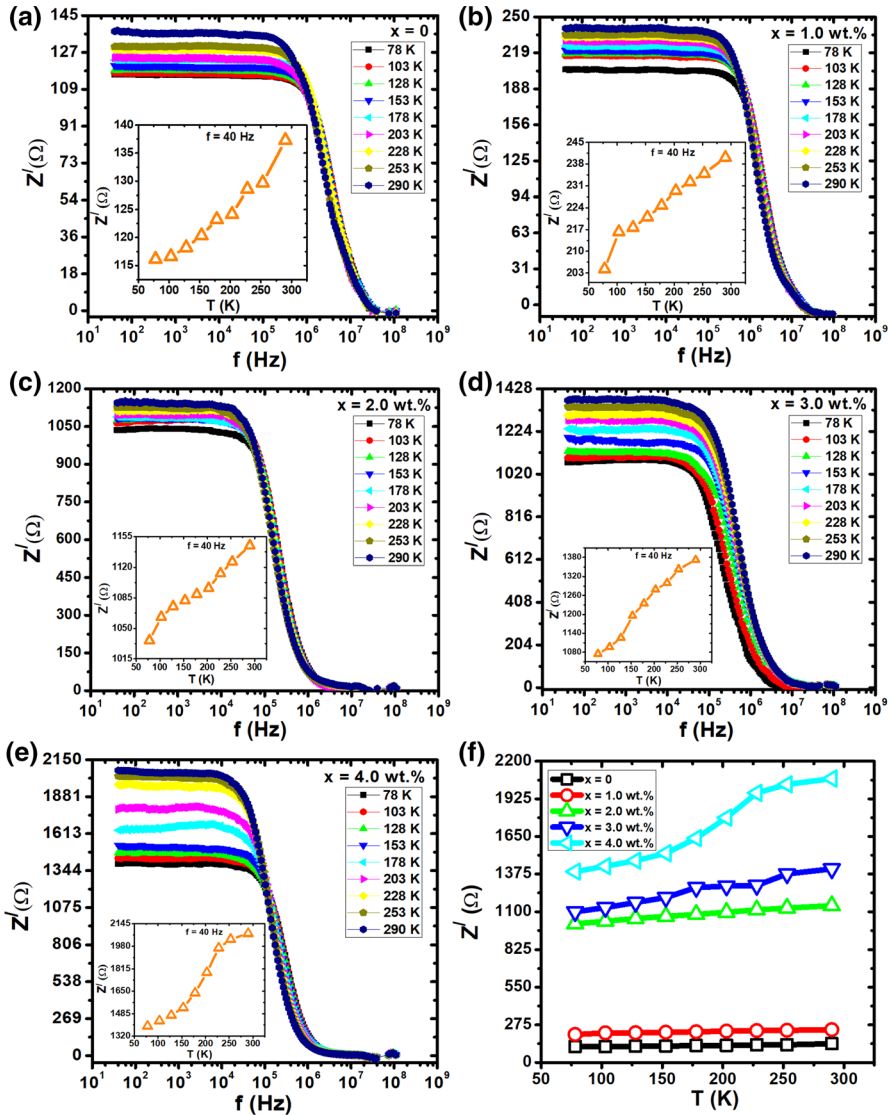
Fig. 11 Variation in real part of impedance Z' (Ω)versus frequency f (Hz) from 40 Hz to 10 MHz for $(Cu)_x$/CuTl-1223 composites with **a** $x=0$ at $T=78$–290 K, **b** $x=1.0$ wt.% at $T=78$–290 K, **c** $x=2.0$ wt% at $T=78$–290 K, **d** $x=3.0$ wt% at $T=78$–290 K, **e** $x=4.0$ wt% at $T=78$–290 K (the insets show the variation in Z' (Ω) versus operating temperature (T) at frequency of 40 Hz), and **f** combined plots of variation in Z' (Ω) versus operating temperatures T (K) at frequency of 40 Hz (Color figure online)

to vary from -4.1×10^1, -1.0×10^2, -4.91×10^2, -5.21×10^2 and -9.12×10^2 at 290 K for $(Cu)_x$/(CuTl)-1223 composites with $x=0$, 1.0, 2.0, 3.0 and 4.0 wt% of Cu NPs, respectively. The shift in the peaks of Z'' (Ω) versus f (Hz) graphs toward lower frequency side has also been observed with increasing T (K), which
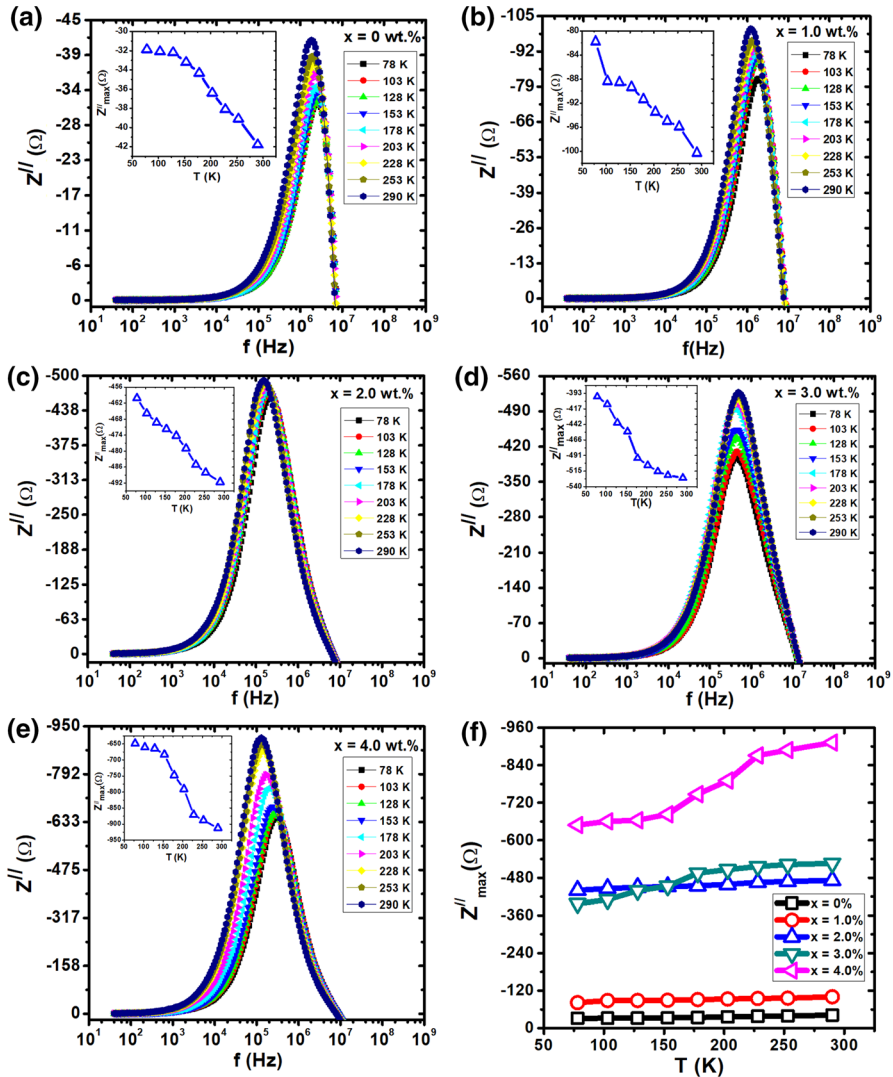
Fig. 12 Variation in imaginary part of impedance Z'' (Ω) versus frequency f (Hz) from 40 Hz to 10 MHz for (Cu)$_x$/CuTl-1223 composites with **a** $x=0$ at $T=78$–290 K, **b** $x=1.0$ wt% at $T=78$–290 K, **c** $x=2.0$ wt% at $T=78$–290 K, **d** $x=3.0$ wt% at $T=78$–290 K, **e** $x=4.0$ wt% at $T=78$–290 K (the insets show the variation in Z''_{max} (Ω) versus operating temperature T (K)), and **f** combined plots of variation in Z''_{max} (Ω) versus operating temperatures T (K) (Color figure online)

shows occurrence of multirelaxation processes in the material. The region below the peaks of Z'' (Ω) versus f (Hz) graphs defines the frequency range in which the mobility of carriers takes place due to long-range hopping. The mobile carriers are restricted to the potential wells at the frequencies beyond the peak maximum (i.e., higher frequencies). The particular frequency at which the peak occurs is an indicative of the transition from long-range to short-range mobility

of carriers. This type of behavior proposes the existence of thermally activated hopping mechanism for AC conduction process (charge transport) in the material [55]. The appearance of peaks in $Z^{//}$ (Ω) versus f (Hz) graphs is a clear sign of the existence of real dielectric relaxation process, and broadening of these peaks demonstrates the spread of relaxation time constant distribution [56]. The combined graph of the variation in $Z^{//}_{max}$ (Ω) versus T (K) for $(Cu)_x/(CuTl)$-1223 composites is shown Fig. 12f. The increasing Cu NPs contents in (CuTl)-1223 matrix have increased the value of $Z^{//}_{max}$ (Ω). The values of $Z^{//}_{max}$ (Ω) varied from -3.1×10^1 to -4.1×10^1, -8.1×10^1 to -1.0×10^2, -4.6×10^2 to -4.91×10^2, -3.98×10^2 to -5.21×10^2 and -6.48×10^2 to -9.12×10^2 with the increase in temperature from 78 to 290 K for $(Cu)_x/(CuTl)$-1223 composites with $x = 0$, 1.0, 2.0, 3.0 and 4.0 wt. %, respectively. The curves indicated that the relaxation has been slightly shifted toward lower frequency regime with the addition of these Cu NPs in the bulk CuTl-1223 phase. Equation (13) explains the shifting of peak positions toward lower frequency (i.e., the increase in the values of C_{gb} and R_{gb} is the cause of the shifting of peaks toward lower frequency)

$$\omega = 2\pi f = \frac{1}{\tau} = \frac{1}{C_{gb}R_{gb}} \tag{13}$$

The increasing values of C_{gb} and R_{gb} increase the relaxation time (τ) and cause the shifting of peaks toward lower frequencies [55, 56]. The shifting of peaks toward lower frequencies is an evidence of the existence of non-Debye relaxation with the decrease in AC conductivity in the material [31, 56].

3.5 Complex Electric Modulus (CEM)

The CEM spectroscopy is a potent tool to separate out the effects of grain and grain boundaries on capacitive contribution, localized dielectric relaxation and long-range conduction, electrical relaxation process in ionic solids and information about nature of polycrystalline materials [27, 57–59]. It can also distinguish the components having different capacitance and same resistance values. The CEM measurements were performed on $(Cu)_x/(CuTl)$-1223 samples at different T (K) values in frequency range from 40 Hz to 10 MHz to explore the relaxation and conduction processes in the material. An equivalent electrical circuit consisting of two subcircuits (i.e., one for grains and other for grain boundaries) has been modeled to analyze CEM measurements data as shown in Fig. 8f. The complex electric modulus (M^*) in terms of $M^/$ and $M^{//}$ can be written in Eq. (14) given below [60]:

$$M^* = M^/ + jM^{//} = j\omega C Z^* \tag{14}$$

The complex impedance (Z^*) in terms of grains and grain boundaries resistances (R_g and R_{gb}) and capacitances (C_g and C_{gb}) from the equivalent electric circuit shown in Fig. 8f can be written as:

$$Z^* = \frac{R_g}{1 + j\omega C_g R_g} + \frac{R_{gb}}{1 + j\omega C_{gb} R_{gb}} \tag{15}$$

Equation 14 can be written as:

$$M^* = j\omega C_o \left(\frac{R_g}{1 + j\omega C_g R_g} + \frac{R_{gb}}{1 + j\omega C_{gb} R_{gb}} \right) \tag{16}$$

where M' and M'' are the real and imaginary parts of complex Modulus M^*:

$$M' = \left[\frac{C_o}{C_g} \left(\frac{(\omega C_g R_g)^2}{1 + (\omega C_g R_g)^2} \right) + \frac{C_o}{C_{gb}} \left(\frac{(\omega C_{gb} R_{gb})^2}{1 + (\omega C_{gb} R_{gb})^2} \right) \right] \tag{17}$$

$$M'' = \left[\frac{C_o}{C_g} \left(\frac{\omega C_g R_g}{1 + (\omega C_g R_g)^2} \right) + \frac{C_o}{C_{gb}} \left(\frac{\omega C_{gb} R_{gb}}{1 + (\omega C_{gb} R_{gb})^2} \right) \right] \tag{18}$$

where C_o is a geometrical capacitance [14]. The frequency-dependent M' versus M'' Nyquist plots for $(Cu)_x$/(CuTl)-1223 composites at different T (K) values are shown in Fig. 13a–e. The left cutoff point on M'-axis of the semicircle of Nyquist plots gives the values of C_g only grains capacitance, while the right cutoff point on the same M'-axis designates the total capacitance $C = C_{gb} + C_g$ of both grain boundaries and grains in the material. The calculated values of 'C_{gb}' and 'C_g' for $(Cu)_x$/(CuTl)-1223 composites at different values of T (K) are given in Table 2. The values of 'C_{gb}' are found to be greater than those of 'C_g' as given in Table 2, which reflects the poor conducting nature of grain boundaries as compared to grains. The presence of different types of imperfections at the grain boundaries makes them relatively less conducting compared to good conducting grains [29, 30]. The enhancement in capacitive behavior can be attributed to the increase in polarization due to trapping of mobile carriers in the potential wells across the grain boundaries promoted by different defects like oxygen vacancies after insertion of Cu NPS in (CuTl)-1223 matrix. The existence of multi-Debye relaxation phenomena can be evident from the temperature-dependent capacitive response of the material, which can be visualized from the change in Nyquist plots with the change in temperature. The total capacitance of grain boundaries has been reduced with rising the values of T (K) for $(Cu)_x$/(CuTl)-1223 composites as given in Table 2. The reduction of capacitance with the rise in temperature may be due to the release of space charges trapped in the potential wells across the intergranular spaces [60].

The plots showing the variation in M' with f (Hz) at different T (K) values are given in Fig. 14a–e. The values of M' at lower frequencies are very small showing negligible capacitive response [31]. The smaller values of M' at lower frequencies demonstrate that AC conduction process is attributed to the long-range mobility of carriers and the contribution of electrode polarization is negligible to the net polarization of the material. The values of M' start to increase at certain frequencies and reach maximum asymptotic values for all temperatures, which is an evidence for the
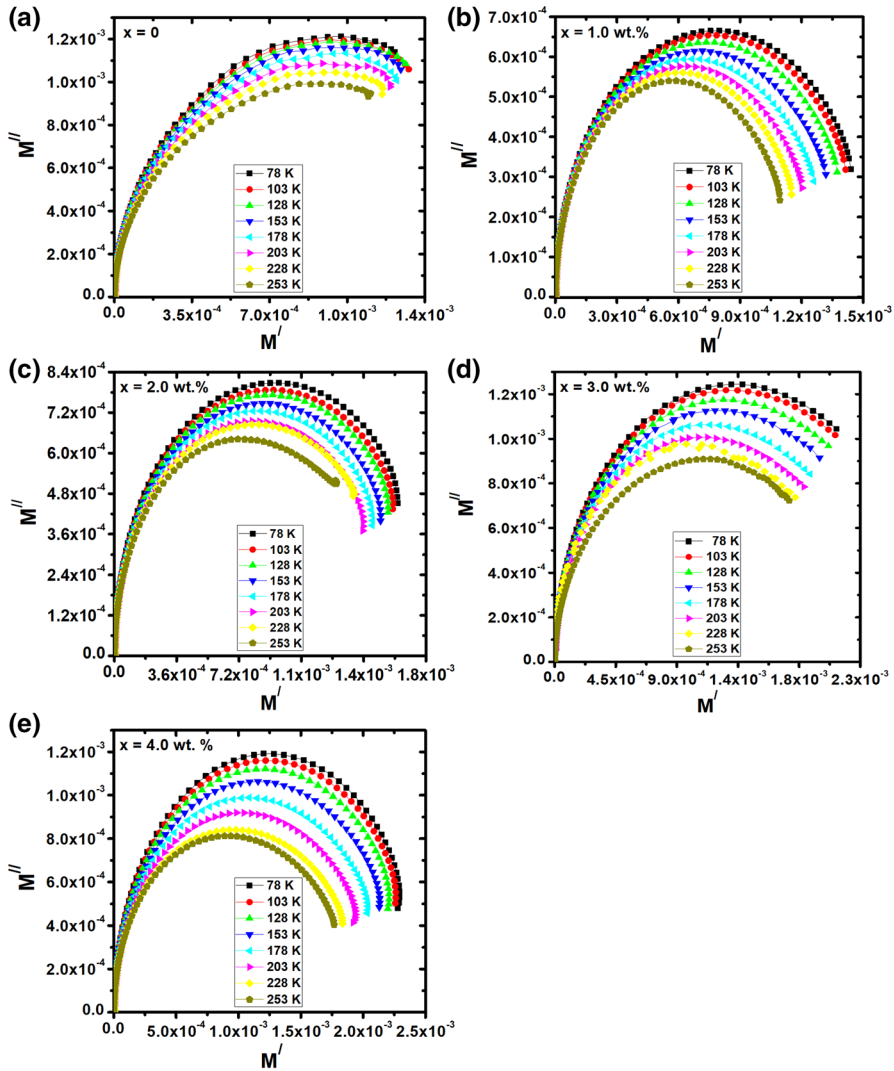
Fig. 13 Nyquist plots between real part (M') and imaginary part (M'') of electric modulus at different operating temperatures T (K) from 78 to 253 K for $(Cu)_x$/CuTl-1223 nanoparticles–superconductor composites with **a** $x=0$, **b** $x=1.0$ wt%, **c** $x=2.0$ wt%, **d** $x=3.0$ wt%, **e** $x=4.0$ wt% (Color figure online)

contribution of short-range mobility of charge carriers in the conduction process. An induced electric field causes the short-range mobility due to a lack of restoring force on the carriers in the material. The value of M' starts to decrease after reaching its maximum value at certain frequency, which is an indicative of transition from long-range to short-range mobility of carriers in the material. The appearance of peak is an evidence of the maximum conductance at certain frequency resulting in the decrease in capacitive response of the material. The plots in the insets of Fig. 14a–e

Table 2 Calculated values of 'C_g' and 'C_{gb}' of $(Cu)_x$/CuTl-1223, $x = 0$, 1.0, 2.0, 3.0 and 4.0 wt% nanoparticles–superconductor composites at various temperatures from 78 to 253 K

| T (K)	$(Cu)_x$/CuTl-1223 composites									
	$x = 0$		$x = 1.0$ wt%		$x = 2.0$ wt%		$x = 3.0$ wt%		$x = 4.0$ wt%	
	C_g (nF)	C_{gb} (mF)	C_g (nF)	C_{gb} (mF)	C_g (nF)	C_{gb} (mF)	C_g (nF)	C_{gb} (mF)	C_g (nF)	C_{gb} (mF)
78	0.091	1.33	0.491	1.44	3.33	1.63	3.66	2.08	4.41	2.27
103	0.086	1.31	0.393	1.42	3.24	1.61	3.47	1.96	3.81	2.24
128	0.075	1.130	0.291	1.37	3.11	1.58	2.34	1.86	3.43	2.18
153	0.063	1.28	0.255	1.32	2.84	1.54	3.13	1.73	3.26	2.11
178	0.042	1.127	0.153	1.26	2.71	1.49	2.86	1.75	2.89	2.02
203	0.034	1.124	0.140	1.22	2.46	1.44	2.67	1.64	2.82	1.93
228	0.028	1.121	0.147	1.15	2.38	1.38	2.46	1.51	2.63	1.83
253	0.029	1.096	0.123	1.13	2.17	1.28	2.54	1.38	2.58	1.74
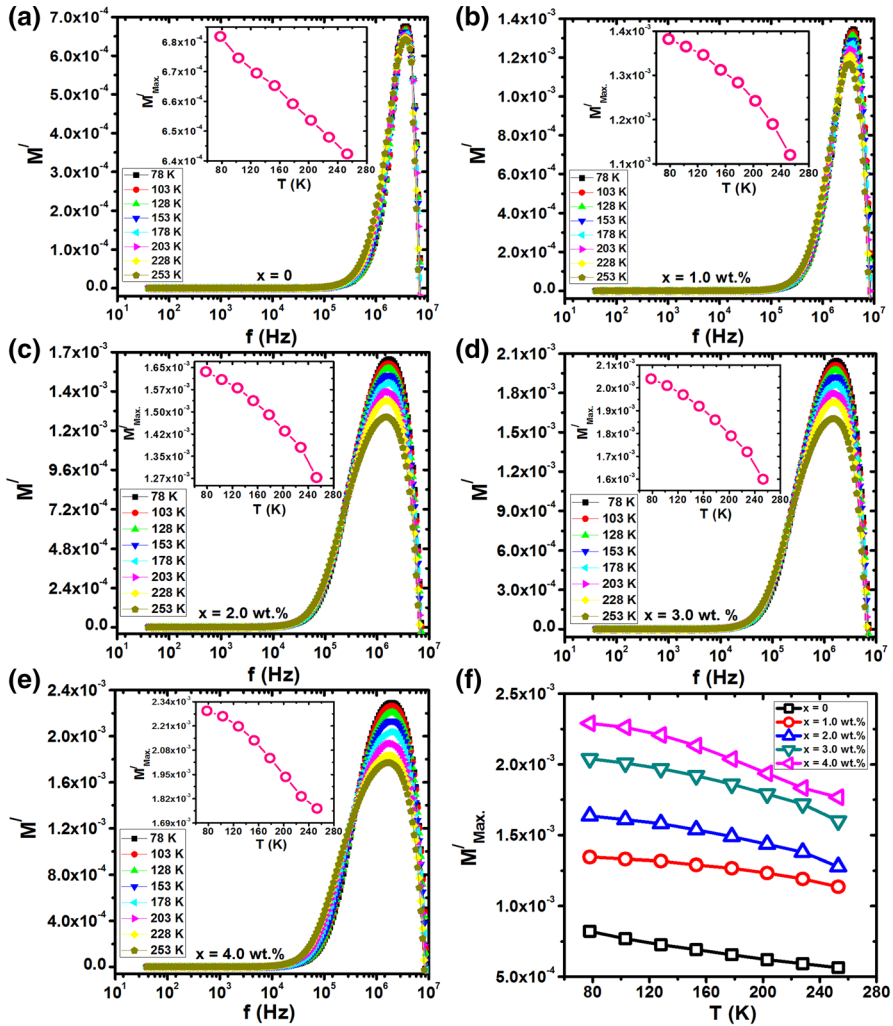
Fig. 14 Variation in real part (M') of electric modulus versus test frequency f (Hz) from 40 Hz to 10 MHz at different operating temperatures T (K) from 78 to 253 K for $(Cu)_x$/CuTl-1223 nanoparticles–superconductor composites with **a** $x=0$, **b** $x=1.0$ wt%, **c** $x=2.0$ wt%, **d** $x=3.0$ wt%, **e** $x=4.0$ wt% each with inset of variation in M'_{Max} versus T (K), and **f** combined variation of M'_{Max} versus T (K) for $(Cu)_x$/CuTl-1223, $x=0$, 1.0, 2.0, 3.0 and 4.0 wt% nanoparticles–superconductor composites (Color figure online)

indicate the gradual decrease in the values of M'_{Max} with the rise in temperature. The value of M'_{Max} decreases from 6.82×10^{-4} to 6.41×10^{-4}, 1.39×10^{-3} to 1.13×10^{-3}, 1.63×10^{-3} to 1.28×10^{-3}, 2.04×10^{-3} to 1.58×10^{-3} and 2.29×10^{-3} to 1.76×10^{-3} for $(Cu)_x$/(CuTl)-1223 composites with $x=0$, 1.0, 2.0, 3.0 and 4.0 wt% of Cu NPs with the increase in T (K) from 78 to 253 K, respectively. The decreasing trend in the values of M'_{Max} indicates the increasing capacitive response due to trapping of

space charges in the potential wells across the grain boundaries promoted with the rise in T (K). The combined plots shown in Fig. 14f demonstrate the increase in the values of $M'_{\mathrm{Max.}}$ with the addition of Cu NPs in CuTl-1223 matrix at all values of T (K), which can be an evidence for enhanced hopping process promoted by the inclusion of Cu nanoparticles at the grain boundaries. The probability of carriers' tunneling through the grain boundaries can be enhanced after addition of conducting Cu NPs in CuTl-1223 matrix.

The frequency-dependent M'' plots at various temperatures are shown in Fig. 15a–e. These plots clearly show the increasing trend of M'' with increasing frequency which reaches its maximum value ($M''_{\mathrm{max.}}$) for all values of T (K). In the insets of Fig. 15a–e, the variation in $M''_{\mathrm{max.}}$ with T (K) is shown. The combined graph showing the variation in $M''_{\mathrm{max.}}$ with T (K) for $(Cu)_x/(CuTl)$-1223 composites is given in Fig. 15f. The value of $M''_{\mathrm{max.}}$ changes from 1.55×10^{-3} to 1.18×10^{-3}, 1.27×10^{-3} to 9.81×10^{-4}, 1.21×10^{-3} to 7.73×10^{-4}, 1.17×10^{-3} to 6.73×10^{-4} and 8.06×10^{-4} to 6.37×10^{-4} at different values of T (K) for $(Cu)_x/(CuTl)$-1223 composites with $x = 0$, 1.0, 2.0, 3.0 and 4.0 wt% of Cu NPs contents, respectively. The value of $M''_{\mathrm{max.}}$ starts to decrease with the increase in frequency with slight shifting of peaks toward lower frequency region with the increase in T (K) values from 78 to 253 K. The appearance of peak showing $M''_{\mathrm{max.}}$ at certain indicates maximum conductance due to long-range hopping process of charge carriers. The carriers are confined to the potential wells at higher frequencies beyond the peak maximum showing the conduction due to mobility of carriers at short distances. The peak is reminiscent of maximum conductance showing a transition from long-range to short-range mobility of carriers with the increasing frequency contributing in AC conduction mechanism. This type behavior can be the indication of thermally activated hopping mechanism contributing to electrical AC conduction or charge transport process in the system [52]. The values of $M''_{\mathrm{max.}}$ were found to be around 1.55×10^{-3}, 1.27×10^{-3}, 1.21×10^{-3}, 1.17×10^{-3} and 8.06×10^{-4} at low temperature of 78 K for $(Cu)_x/(CuTl)$-1223 composites with $x = 0$, 1.0, 2.0, 3.0 and 4.0 wt% of Cu NPs, respectively. The broadening of M'' versus f (Hz) peaks demonstrates the spread of relaxation with relaxation time constant distribution showing the non-Debye nature of the material. The decrease in $M''_{\mathrm{max.}}$ with increasing Cu NPs contents in CuTl-1223 matrix showed the improved capacitive response of the material after the spread of these NPs over the grain boundaries' regions [61]. The slight shifting of peaks toward lower frequency regions is obvious from M'' versus f (Hz) curves after addition of Cu NPs in (CuTl)-1223 matrix. The increase in grain boundaries' capacitance (C_{gb}) and resistance (R_{gb}) can easily explain the shifting of peak positions toward lower frequencies by the following relation mentioned in Eq. 19 given below:

$$\omega = 2\pi f = \frac{1}{\tau} = \frac{1}{C_{\mathrm{gb}}R_{\mathrm{gb}}} \tag{19}$$

By increasing the values of 'R_{gb}' and 'C_{gb},' the relaxation time (τ) increases, which causes the shifting of peaks toward lower frequency. The gradual decrease
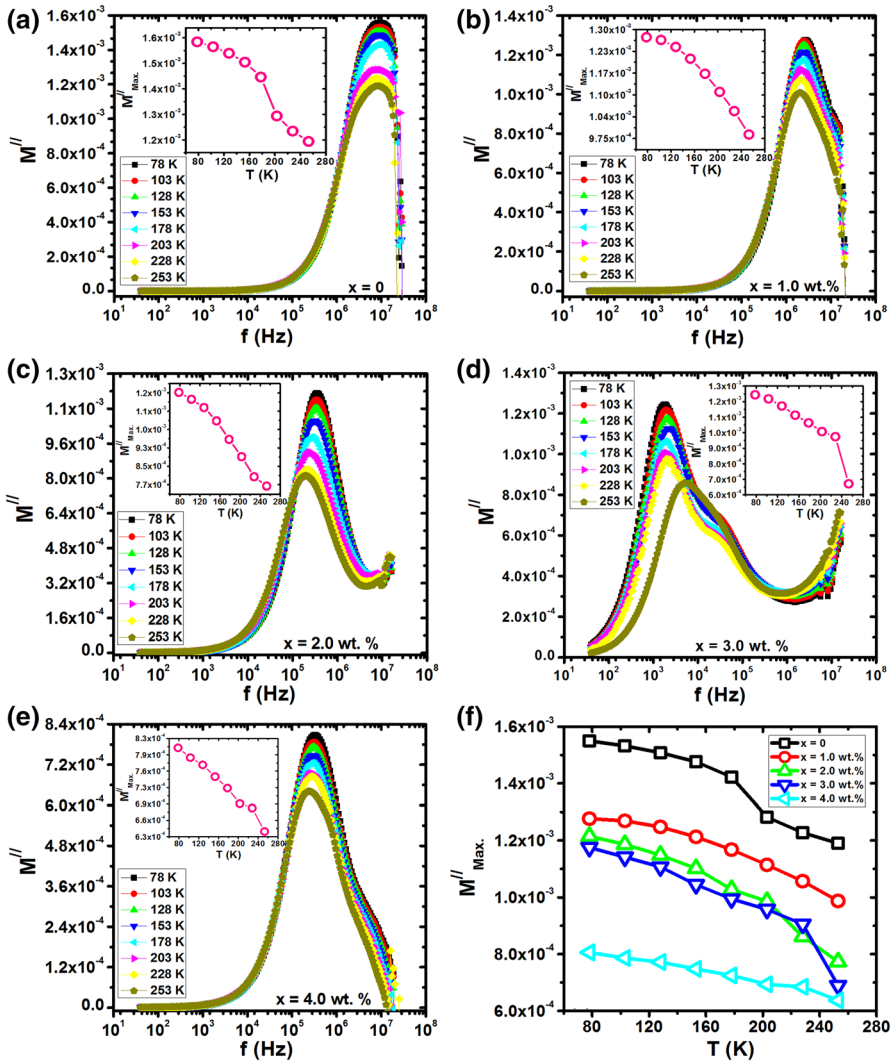
Fig. 15 Variation in imaginary part (M'') of modulus versus test frequency f (Hz) from 40 Hz to 10 MHz at different operating temperatures T (K) from 78 to 253 K for $(Cu)_x$/CuTl-1223 nanoparticles–superconductor composites with **a** $x=0$, **b** $x=1.0$ wt%, **c** $x=2.0$ wt%, **d** $x=3.0$ wt%, **e** $x=4.0$ wt% each with inset of variation in M''_{max} versus T (K), and **f** combined variation in M''_{max} versus T (K) for $(Cu)_x$/CuTl-1223, $x=0$, 1.0, 2.0, 3.0 and 4.0 wt% nanoparticles–superconductor composites (Color figure online)

in M'' versus f (Hz) peaks intensities demonstrates the decrease in AC conductance and increase in capacitive response of the material with the increase in temperature. Shifting of these peaks toward lower frequency side witnessed the increase in relaxation time.

4 Conclusion

The frequency- and temperature-dependent AC conduction process was explored via dielectric, impedance and electric modulus measurements of $(Cu)_x$/(CuTl)-1223 composites. The XRD spectrum of Cu NPs revealed single-phase FCC crystal structure without any impurity. The tetragonal crystal structure with P4/mmm space group of the host (CuTl)-1223 superconducting phase remained dominant after the addition of Cu NPs. The unaltered crystal structure indicated the dispersion of Cu NPs across the grain boundaries of (CuTl)-1223 superconducting phase. The normal state resistivity ρ (Ω m) was decreased, while zero-resistivity critical temperature $T_{c(0)}$ (K) was increased after the insertion of Cu NPs in (CuTl)-1223 phase. This improvement in superconducting properties could be associated with the enhanced mobility of carriers and superconducting volume fraction due to the presence of conducting Cu NPs over the intergranular spaces of (CuTl)-1223 matrix. The dielectric constants (ε_r', ε_r''), and loss tangent (tanδ) were suppressed, while AC conductivity (σ_{ac}) was improved with the addition of Cu NPs in (CuTl)-1223 matrix, which could be associated with the suppression of polarization in the material. The frequency-dependent CIS measurements at different temperatures suggested the thermally activated hopping mechanism responsible for electrical AC conduction (charge transport) process in $(Cu)_x$/(CuTl)-1223 composites. The increase in the resistances of grains and grain boundaries with the increase in temperature was witnessed for the conducting nature of grains and grain boundaries promoted with the addition of Cu NPs in (CuTl)-1223 system. Similarly, frequency-dependent CEM measurements of $(Cu)_x$/(CuTl)-1223 composites at different temperatures indicated that both the grains and grain boundaries had affected the AC conduction properties. The trapped space charges in the potential wells across the grain boundaries were released with the rise of T (K), which was the main source of suppression of capacitive response of the material. The shifting of peaks in the spectra of Z'' (Ω) versus f (Hz) and M'' versus f (Hz) toward lower frequencies with increasing contents of metallic Cu NPs showed the existence of non-Debye type of relaxation processes in the material. The greater values of resistance and capacitance of grain boundaries as compared to grains showed the poor conducting nature of grain boundaries of the material. This study can be helpful to figure out the different factors contributing to AC conduction processes and to explore the effects of nanostructures dispersed at the grain boundaries in AC conduction mechanism of the system.

References

1. M. Hasan, M.C. Nguyen, H. Kim, S.W. You, Y.S. Jeon, D.T. Tong, D.H. Lee, J.K. Jeong, R. Choi, High performance solution processed zirconium oxide gate dielectric appropriate for low temperature device application. Thin Solid Films **589**, 90 (2015)
2. T.F. Zhang, X.G. Tang, Q.X. Liu, Y.P. Jiang, L.L. Jiang, L. Luo, Optical and dielectric properties of PbZrO$_3$ thin films prepared by a sol–gel process for energy storage application. Mater. Des. **90**, 410 (2016)

3. M. Jarvid, A. Johansson, R. Kroon, J.M. Bjuggren, H. Wutzel, V. Englund, S. Gubanski, M.R. Andersson, C. Muller, A new application area for fullerenes: voltage stabilizers for power cable insulation. Adv. Mater. **27**, 897 (2015)

4. N.A. Khan, M. Mumtaz, A.A. Khurram, Frequency dependent dielectric properties of $Cu_{0.5}Tl_{0.5}Ba_2Ca_2Cu_{3-y}Zn_yO_{10-\delta}$ ($y=0$, 1.0, 1.5, 2.0, 2.5) superconductors. J. Appl. Phys. **104**, 033916 (2008)

5. P. Ben-Ishai, E. Sader, Y. Feldman, I. Felner, M. Weger, Dielectric properties of $Na_{0.7}CoO_2$ and of the superconducting $Na_{0.3}CoO_2 \cdot 1.3\ H_2O$. J. Supercond. **18**, 455 (2005)

6. C.M. Rey, H. Mathias, L.R. Testardi, S. Skirius, High dielectric constant and nonlinear electric response in nonmetallic $YBa_2Cu_3O_{6+\delta}$. Phys. Rev. B **45**, 10639 (1992)

7. L.L. Hench, J.K. West, *Principles of Electronic Ceramics*, 1st edn. (Wiley, New York, 1990)

8. L. Li, C. Richter, S. Paetel, T. Kopp, J. Mannhart, R.C. Ashoori, Very large capacitance enhancement in two-dimensional electron system. Science **332**, 825 (2011)

9. H. Ihara, How to achieve the best performance superconductor based on Cu-1234. Physica C **364–365**, 289 (2001)

10. X. Xu, Z. Jiao, M. Fu, L. Feng, K. Xu, R. Zuo, X. Chen, Dielectric studies in a layered Ba based Bi-2222 cuprate $Bi_2Ba_2Nd_{1.6}Ce_{0.4}Cu_2O_{10+\delta}$. Physica C **417**, 166 (2005)

11. S. Cavdar, H. Koralay, N. Tugluoglu, A. Gunen, Frequency-dependent dielectric characteristics of Tl–Ba–Ca–Cu–O bulk superconductor. Supercond. Sci. Technol. **18**, 1204 (2005)

12. R.K. Nkum, M.O. Gyekye, F. Boakye, Normal-state dielectric and transport properties of in-doped Bi–Pb–Sr–Ca–Cu–O. Solid State Commun. **122**, 569 (2002)

13. N.H. Mohammad, Effect of MgO nano-oxide additions on the superconductivity and dielectric properties of $Cu_{0.25}Tl_{0.75}Ba_2Ca_3Cu_4O_{12-\delta}$ superconducting phase. J. Supercond. Nov. Magn. **25**, 45 (2012)

14. J.R. Macdonald, *Impedance Spectroscopy, Emphasizing Solid Materials and Systems* (Wiley, New York, 1987)

15. W. Hao, J. Zhang, Y. Tan, W. Su, Giant dielectric-permittivity phenomena of compositionally and structurally $CaCu_3Ti_4O_{12}$-like oxide ceramics. J. Am. Ceram. Soc. **92**, 2937 (2009)

16. D. Szwagierczak, Dielectric behavior of $Bi_{2/3}Cu_3Ti_4O_{12}$ ceramic and thick films. J. Electroceram. **23**, 56 (2009)

17. L. Singh, U.S. Rai, K.D. Mandal, N.B. Singh, Progress in the growth of $CaCu_3Ti_4O_{12}$ and related functional dielectric perovskites. Prog. Cryst. Growth Charact. Mater. **60**, 15 (2014)

18. M.A. Subramanian, D. Li, N. Duan, B.A. Reisner, A.W. Sleight, High dielectric constant in $ACu_3Ti_4O_{12}$ and $ACu_3Ti_3FeO_{12}$. J. Solid State Chem. **151**, 323 (2000)

19. A. Bagum, M.B. Hossen, F.U.Z. Chowdhury, Complex impedance and electric modulus studies of Al substituted $Co_{0.4}Cu_{0.2}Zn_{0.4}Al_xFe_{2-x}O_4$ ferrites prepared by auto combustion technique. J. Ferroelectr. **494**, 19 (2016)

20. S.A. Nedilko, I.V. Fesych, O.G. Dzyazko, A.S. Bulachok, S.O. Solopan, T.O. Plutenko, Synthesis of barium cuprate by secondary induction heating and its electrical properties. Powder Metall. Met. Ceram. **55**, 347 (2016)

21. J. Bashir, R. Shaheen, Structural and complex AC impedance spectroscopic studies of A_2CoNbO_6 (A = Sr, Ba) ordered double perovskites. Solid State Sci. **13**, 993 (2011)

22. P. Liang, Z. Yang, X. Chao, Improved dielectric properties and grain boundary response in neodymium-doped $Y_{2/3}Cu_3Ti_4O_{12}$ ceramics. J. Alloys Compd. **678**, 273 (2016)

23. B. Behera, P. Nayak, R.N.P. Choudhary, Structural and impedance properties of $KBa_2V_5O_{15}$ ceramics. Mater. Res. Bull. **43**, 401 (2008)

24. A.P. Sakhya, A. Dutta, T.P. Sinha, Dielectric and impedance spectroscopic studies of neodymium gallate. Physica B **488**, 1 (2016)

25. S. Thakur, R. Rai, I. Bdikin, M.A. Valentec, Impedance and modulus spectroscopy characterization of Tb modified $Bi_{0.8}A_{0.1}Pb_{0.1}Fe_{0.9}Ti_{0.1}O_3$ ceramics. Mater. Res. **19**, 1 (2016)

26. F. Tian, Y. Ohki, Electric modulus powerful tool for analyzing dielectric behavior. IEEE Trans. Dielectr. Electr. Insul. **21**, 929 (2014)

27. B.H. Venkataraman, K.B.R. Varma, Microstructural, dielectric, impedance and electric modulus studies on vanadium-doped and pure strontium bismuth niobate $(SrBi_2Nb_2O_9)$ ceramics. J. Mater. Sci. Mater. Electron. **16**, 335 (2005)

28. A.R. West, M.A. Verges, Impedance and modulus spectroscopy of ZnO varistors. J. Electroceram. **1**, 125 (1997)

29. A.M. Nawar, H.M. Abd El-Khalek, M.M. El-Nahass, Dielectric and electric modulus studies on Ni(II) tetra-phenyl porphyrin thin films. Org. Opto-Electr. **1**, 25 (2015)

30. A.K. Roy, K. Prasad, A. Prasad, Piezoelectric, impedance, electric modulus and AC conductivity studies on $(Bi_{0.5}Na_{0.5})_{0.95}Ba_{0.05}TiO_3$ ceramics. Proc. Appl. Ceram. **7**, 81 (2013)

31. M.B. Hossen, A.K.M.A. Hossain, Complex impedance and electric modulus studies of magnetic ceramic $Ni_{0.27}Cu_{0.10}Zn_{0.63}Fe_2O_4$. J. Adv. Ceram. **4**, 217 (2015)

32. N. Murali, S.J. Margarette, V.K. Rao, V. Veeraiah, Structural, impedance, dielectric and modulus analysis of $LiNi_{1-x-y-0.02}Mg_{0.02}Co_xZn_yO_2$ cathode materials for lithium-ion batteries. J. Sci. Adv. Mater. Dev. **2**, 233 (2017)

33. P.S. Sahoo, A. Panigrahi, S.K. Patri, R.N.P. Choudhary, Impedance and modulus spectroscopy studies of $Ba_4SrSmTi_3V_7O_{30}$ ceramics. Mater. Sci. Pol. **28**, 763 (2010)

34. N. Padmamalini, K. Ambujam, Impedance and modulus spectroscopy of ZrO_2–TiO_2–V_2O_5 nanocomposites. Karbala Int. J. Mod. Sci. **2**, 271 (2016)

35. R. Kundu, D. Roy, S. Bhattacharya, Microstructure, electrical conductivity and modulus spectra of CdI_2 doped nanocomposite-electrolytes. Physica B **507**, 107 (2017)

36. Y. Suresh, S. Annapurna, A.K. Singh, G. Bhikshamaiah, Green synthesis and characterization of tea decoction stabilized copper nanoparticles. Int. J. Innov. Res. Sci. Eng. Technol. **3**, 11265 (2014)

37. L. Ali, M. Mumtaz, I. Ali, M. Waqee-ur-Rehman, A. Jabbar, Metallic Cu nanoparticles added to $Cu_{0.5}Tl_{0.5}Ba_2Ca_2Cu_3O_{10-\delta}$ superconductor. J. Supercond. Nov. Magn. **31**, 561 (2018)

38. K.C. Kao, *Dielectric Phenomena in Solids*, 1st edn. (Elsevier Academic Press, Amsterdam, 2004)

39. H.M. El-Mallah, AC-electrical conductivity and dielectric properties of perovskite (Pb, Ca)TiO_3 ceramic. Acta Phys. Pol. A **122**, 174 (2012)

40. K.W. Wagner, Theory of imperfect dielectrics. Ann. Phys. **345**, 817 (1913)

41. C.G. Koops, On the dispersion of resistivity and dielectric constant of some semiconductors at audio frequencies. Phys. Rev. **83**, 121 (1951)

42. W. Cao, R. Gerhardt, Calculation of various relaxation times and conductivity for a single dielectric relaxation process. Solid State Ion. **42**, 213 (1990)

43. B. Tareev, *Physics of Dielectric Material* (Mir Publisher, Moscow, 1975)

44. T.G. Abdel-Malak, M.E. Kassem, N.S. Aly, S.M. Kalil, AC conductivity of cobalt phthalocyanine. Acta Phys. Pol. A **81**, 675 (1992)

45. R. Singh, R.P. Tandon, V.S. Panwar, S. Chandra, Low frequency ac conduction in lightly doped polypyrrole films. J. Appl. Phys. **69**, 2504 (1991)

46. H.M. Ragab, Studies on the thermal and electrical properties of polyethylene oxide/polyvinyl alcohol blend by incorporating of cesium chloride. Res. Phys. **7**, 2057 (2017)

47. J. Hou, R. Vaish, Y. Qu, D. Krsmanovic, K.B.R. Varma, R.V. Kumar, Dielectric relaxation and electrical conductivity in Bi_5NbO_{10} oxygen ion conductors prepared by a modified sol–gel process. J. Power Sources **195**, 2613 (2010)

48. J.R. Macdonald, L.D. Potter Jr., A flexible procedure for analyzing impedance spectroscopy results: description and illustrations. Solid State Ion. **24**, 61 (1987)

49. M. Kaiser, Electrical conductivity and complex electric modulus of titanium doped nickel–zinc ferrites. Physica B **407**, 606 (2012)

50. N.G. Mccrum, B.E. Read, G. Williams, *Anelastic and Dielectric Effects in Polymeric Solids* (Wiley, New York, 1967)

51. C.T. Moynihan, Analysis of electrical relaxation in glasses and melts with large concentrations of mobile ions. J. Non-Cryst. Solids **172–174**, 1395 (1994)

52. J. Liu, C.-G. Duan, W.-G. Yin, W.N. Mei, R.W. Smith, J.R. Hardy, Large dielectric constant and Maxwell–Wagner relaxation in $Bi_{2/3}Cu_3Ti_4O_{12}$. Phys. Rev. B **70**, 144106 (2004)

53. H. Rahmouni, M. Smari, B. Cherif, E. Dhahri, K. Khirouni, Conduction mechanism, impedance spectroscopic investigation and dielectric behavior of $La_{0.5}Ca_{0.5-x}Ag_xMnO_3$ manganites with compositions below the concentration limit of silver solubility in perovskites ($0 \leq x \leq 0.2$). Dalton Trans. **44**, 10457 (2015)

54. S. Nasri, A.L.B. Hafsia, M. Tabllout, M. Megdiche, Complex impedance, dielectric properties and electrical conduction mechanism of $La_{0.5}Ba_{0.5}FeO_{3-\delta}$ perovskite oxides. RSC Adv. **6**, 76659 (2016)

55. K. Lily, K. Prasad, R.N.P. Choudhary, Impedance spectroscopy of $(Na_{0.5}Bi_{0.5})(Zr_{0.25}Ti_{0.75})O_3$ lead free ceramic. J. Alloys Compd. **453**, 325 (2008)

56. I. Ahmad, M.J. Akhtar, M. Younas, M. Saddique, M.M. Hasan, Small polaronic hole hopping mechanism and Maxwell–Wagner relaxation in $NdFeO_3$. J. Appl. Phys. **112**, 074105 (2012)

57. K. Prasad, A. Kumar, S.N. Choudhary, R.N.P. Choudhary, Relaxor behavior of Pb[(Mg$_{3/4}$Co$_{1/4}$)$_{1/3}$Nb$_{2/3}$]O$_3$ ceramic. Solid State Ion. **176**, 1641 (2005)
58. P.B. Macedo, C.T. Moynihan, R. Bose, The role of ionic diffusion in polarisation in vitreous ionic conductors. Phys. Chem. Glasses **13**, 171 (1972)
59. R. Gerhardt, Impedance and dielectric spectroscopy revisited: distinguishing localized relaxation from long-range conductivity. J. Phys. Chem. Solids **55**, 1491 (1994)
60. J. Liu, C.-G. Duan, W.-G. Yin, W.N. Mei, R.W. Smith, J.R. Hardy, Dielectric permittivity and electric modulus in Bi$_2$Ti$_4$O$_{11}$. J. Chem. Phys. **119**, 2812 (2003)
61. M. Naveed, M. Mumtaz, R. Khan, A.A. Khan, M. Nasir Khan, Conduction mechanism and impedance spectroscopy of (MnFe$_2$O$_4$)$_x$/CuTl-1223 nanoparticle–superconductor composites. J. Alloys Compd. **712**, 696 (2017)

Affiliations

Abrar A. Khan[1] · M. Mumtaz[1] · Liaqat Ali[1] · Mubasher[1] · Y. Slimani[2] · M. Nasir Khan[3] · Irfan Qasim[4]

[1] Materials Research Laboratory, Department of Physics, Faculty of Basic and Applied Sciences (FBAS), International Islamic University (IIU), Islamabad 44000, Pakistan

[2] Department of Biophysics, Institute for Research and Medical Consultations (IRMC), Imam Abdulrahman Bin Faisal University, P.O. Box 1982, Dammam 31441, Saudi Arabia

[3] Central Diagnostic Laboratory, Physics Division, PINSTECH, Islamabad 45500, Pakistan

[4] Department of Physics, Riphah International University, Islamabad, Pakistan